

1 **Monitoring crater-wall collapse at active volcanoes: a study of the 12 January 2013 event at**
2 **Stromboli**

3 Sonia Calvari^{1*}, Emanuele Intrieri², Federico Di Traglia², Alessandro Bonaccorso¹, Nicola Casagli²,
4 Antonio Cristaldi¹

5

6 1 - Istituto Nazionale di Geofisica e Vulcanologia, Osservatorio Etneo - Sezione di Catania, Piazza
7 Roma 2, 95125 Catania, Italy

8 2 - Dipartimento di Scienze della Terra, Università di Firenze, Via La Pira 4, 50121, Firenze, Italy

9

10 *Corresponding author - Sonia Calvari: sonia.calvari@ingv.it

11 Emanuele Intrieri: emanuele.intrieri@unifi.it

12 Federico Di Traglia: federico.ditraglia@unifi.it

13 Alessandro Bonaccorso: alessandro.bonaccorso@ingv.it

14 Nicola Casagli: nicola.casagli@unifi.it

15 Antonio Cristaldi: antonio.cristaldi@ingv.it

16

17

18 **Keywords:** Stromboli volcano; remote sensing; visible and infrared webcam monitoring; ground-
19 based radar interferometry; crater-wall collapse; volcano instability.

Abstract

Crater-wall collapses are fairly frequent at active volcanoes, and they are normally studied through the analysis of their deposits. In this paper, we present an analysis of the 12 January 2013 crater-wall collapse occurring at Stromboli volcano, investigated by means of a monitoring network comprising visible and infrared webcams and a Ground-Based Interferometric Synthetic Aperture Radar. The network revealed the triggering mechanisms of the collapse, which are comparable to the events that heralded the previous effusive eruptions in 1985, 2002, 2007 and 2014. The collapse occurred during a period of inflation of the summit cone and was preceded by increasing explosive activity and the enlargement of the crater. Weakness of the crater wall, increasing magmatic pressure within the upper conduit induced by ascending magma, and mechanical erosion caused by vent opening at the base of the crater wall and by lava fingering, are considered responsible for triggering the collapse on 12 January 2013 at Stromboli. We suggest that the combination of these factors might be a general mechanism to generate crater-wall collapse at active volcanoes.

1. Introduction

Crater-wall collapse at active volcanoes is one of the mechanisms generating mass-wasting phenomena such as rock falls, landslides, rock avalanches and/or pyroclastic density currents (Sumner 1998; Robertson et al. 2000; Alvarado and Soto 2002; Calvari and Pinkerton 2002; Behncke et al. 2003, 2008; Cole et al. 2005; Lube et al. 2007; Charbonnier and Gertisser 2009). Studies of crater-wall collapse are usually carried out by geological field analyses of the deposit, and by reconstructing the collapse process and triggering mechanisms from the deposit's features (e.g., Alvarado and Soto 2002; Behncke et al. 2003; Miyabuchi et al. 2006; Cobenas et al. 2012; Eychenne et al. 2013). The increasing use of remote sensing devices in volcano monitoring (e.g. Ripepe et al. 2004; Bertolaso et al. 2008; Spampinato et al. 2011; Harris 2013; Bonforte and Guglielmino 2015) has greatly improved knowledge of the precursory conditions leading to crater-

44 wall failure, and magma emplacement appears to be the primary triggering factor (Sparks et al.
45 2002; Voight et al. 2002; Acocella 2005).

46 Although the deposits associated with such collapses at Stromboli normally spread along the barren
47 Sciara del Fuoco (SdF) slope, and thus do not pose a significant risk to the population, the ash cloud
48 and ballistic block fallout accompanying the hot avalanches might impact on the summit track used
49 by tourists and cause vegetation fires (Rosi et al. 2006; Pistolesi et al. 2011). In addition, since these
50 phenomena are related to the initial phases of eruptive fissure opening, recognising and
51 understanding mechanisms leading to crater-wall collapse play a crucial role in evaluating their
52 potential hazard, and may shed new light on intrusion processes within cinder cones. The data
53 presented here represent the first identification of precursors to crater-wall collapse detected at
54 Stromboli from a monitoring network. They give new insights into summit crater failures, which
55 can evolve into flank effusive eruptions, and provide new possibilities for forecasting such events at
56 this and other volcanoes.

57 In this paper, we have integrated data from the monitoring networks operating at Stromboli volcano
58 (Fig. 1a-b) to constrain the mechanisms leading to the generation of the 12 January 2013 crater-wall
59 collapse. Data comprise the videos recorded by the visible and infrared webcam network (Calvari et
60 al. 2010) and Synthetic Aperture Radar (SAR) imagery from the permanent Ground-Based
61 Interferometric SAR (GBInSAR; Casagli et al. 2009). The aim was to integrate results to identify
62 deformation associated with collapse phenomena, thus improving our understanding of the
63 triggering mechanisms of these events. It was thanks to this monitoring system that these events are
64 now regularly detected, given that their deposits, spread along the steep SdF slope, are rapidly
65 eroded and/or covered by lava flows, or by ejecta erupted from the summit craters during the
66 persistent strombolian activity.

67 **2. Background**

68 *2.1 Shallow dike intrusion, cinder cones, and crater-wall collapses at active volcanoes*

69 Magma can propagate within a volcanic edifice both laterally and vertically, and its propagation
70 depends on the presence of preexisting weakness zones, the shape of the edifice and regional
71 tectonic control (McGuire and Pullen 1989; Tibaldi 1996; Acocella and Neri 2009). Diking and
72 lateral intrusions within scoria cones can form cryptodome structures or massive bulbous intrusions
73 (Behncke et al. 2003; Petronis et al. 2013), and dike widening and outward bulging and flaring has
74 been observed when intruding poorly consolidated rocks (Houghton and Schmincke 1989; Baer
75 1991; Petronis et al. 2013; Geshi and Neri 2014). Observations at active and inactive cinder cones
76 include inward or vertical collapse of the summit cone following magma drainage (e.g., Guest et al.
77 1974; Houghton and Schmincke 1989; Calvari and Pinkerton 2004; Staudacher et al. 2009) and
78 outward displacement of sectors of the summit cone caused by pressure build-up within the crater
79 (Sparks et al. 2002; Voight et al. 2002; Behncke et al. 2003, 2008; Petronis et al. 2013; Wadsworth
80 et al. 2015). Viscous indentation can take place from the central conduit towards the cone flanks,
81 inducing bulging and ephemeral vent opening at the base of the cone (Guest et al. 1974; Behncke et
82 al. 2003; Petronis et al. 2013), and causing tilting and crushing of the surrounding scoria layers
83 (Petronis et al. 2013). Lava flows are generally associated with cinder or spatter cone growth
84 (Slatcher et al. 2015), and proximal spatter can be incorporated in rheomorphic lava flows (Parcheta
85 et al. 2012) thus increasing cone erosion during lava flow emplacement.

86 Widespread avalanching around the summit cone occurred at Vesuvius during its 1944 eruption,
87 where slopes of loose tephra had been preloaded with lava flows or where heavy accumulations of
88 ash were deposited by prevailing winds (Hazlett et al. 1991). About 75% of the cone surface above
89 900 m elevation had been affected by avalanches, which removed $5\text{--}10 \times 10^6 \text{ m}^3$ of material from
90 the top of the cone and reached the maximum distance of $\sim 1.3 \text{ km}$ from the crater rim (Table 1;
91 Hazlett et al. 1991; Cole and Scarpati 2010).

92 Frequent crater-wall collapses at Arenal volcano were triggered by an increase in the magma level
93 within the summit crater and were not associated with explosive activity (Table 1; Alvarado and

94 Soto 2002; Cole et al. 2005). Cole et al. (2005) have noted that collapses at Arenal volcano occurred
95 in a specific region of the crater wall, where there was new magma along fractures and fissures.
96 They attribute the generation of several crater-wall collapses either to lava flow accumulation in the
97 summit region or to internal magma pressurization, especially when preceded by summit ground
98 deformation.

99 Similar but much smaller events took place at the summit of Etna volcano after a phase of high
100 fountaining and dome growing, producing hot avalanches that spread a few hundred meters from
101 the crater rim (Table 1; Calvari and Pinkerton 2002; Behncke et al. 2003). The collapse at Etna
102 occurred once explosive activity ceased, and was facilitated by the undermining effect on the slope
103 caused by intrusion of very viscous lava through parts of the mass flow (Calvari and Pinkerton
104 2002). Another collapse episode was generated during the opening of a large fracture on the flank
105 of SE-Crater summit cone, and involved the collapse of part of the cone, rock falls and pyroclastic
106 density currents that travelled up to 1 km from the source (Behncke et al. 2008).

107 The 26 December 1997 sector collapse at Montserrat produced a violent $\sim 50 \times 10^6 \text{ m}^3$ pyroclastic
108 density current forecasted by increasing seismicity and ground fracturing. It was triggered by failure
109 of the summit lava dome and also involved collapse of the southern flank of the summit crater wall
110 made of talus (Sparks et al. 2002; Voight et al. 2002).

111 The risk posed by crater-wall collapses depends on the distribution of magma within the crater and
112 crater walls, on flank dike intrusion (e.g., Billi et al. 2003), on the morphology of a volcano, on the
113 distribution of the populated areas along its slopes, and on the size of the failure and resulting
114 deposit. In this respect, the availability of an appropriate monitoring system to enable its mitigation
115 is extremely important. To the best of our knowledge, there are rare examples of crater-wall failures
116 monitored through a multidisciplinary array like Stromboli (e.g., Bonforte and Guglielmino 2015).

117 The case-study reported in this paper thus gives new insights on these events and offers new
118 possibilities to prevent them.

119 2.2 *Geologic background*

120 Stromboli is a volcanic island located at the north-easternmost end of the Aeolian Archipelago (Fig.
121 1a-b). It is characterized by persistent strombolian activity (Chouet et al. 1974; Patrick 2007;
122 Patrick et al. 2007; Gaudin et al. 2014; Leduc et al. 2015), with major explosions (i.e. more
123 powerful than the average strombolian explosions; Barberi et al. 1993; Andronico et al. 2008;
124 Calvari et al. 2012; Rosi et al. 2013; Cigolini et al. 2014) normally occurring twice a year
125 (Bertagnini et al. 1999). Extremely rare and powerful explosions called "paroxysms" also affect the
126 villages along the shoreline (Fig. 1b; Rittmann 1931; Calvari et al. 2006; Rosi et al. 2006; Harris et
127 al. 2008; Pistolesi et al. 2011; Bonaccorso et al. 2012). The persistent explosive activity takes place
128 from several vents within the crater terrace, an elliptical depression elongated NE-SW, about 300 m
129 long and 50 m wide located at ~750 m a.s.l. (Fig. 1c). It lies at the headwall of the SdF (Fig. 1b-c), a
130 collapse scar on the NW flank of the island formed during the last 13 ka (Tibaldi 2001). Stromboli
131 is frequently affected by instability phenomena, such as landslides located mainly in the SdF area,
132 which have triggered tsunamis (~1 every 20 years; Rosi et al. 2013). Slope instability phenomena
133 are classified based on their size in types: 1) giant deep-seated gravitational slope deformations like
134 those recognized in the past history of Stromboli (volumes $>10^6$ m³; Tibaldi 2001); 2) shallower,
135 large and more frequent landslides, such as the one occurring in late December 2002, involving
136 loose deposits and rock masses (volumes $\sim 10^6$ m³; Tommasi et al. 2005); 3) very shallow landslides,
137 involving loose or weakly consolidated deposits (volumes $\sim 10^5$ m³), with detachment areas located
138 in the SdF and in the slopes around the crater terrace (Di Traglia et al. 2014b). The crater terrace
139 comprises 3 areas where eruptive vents open (Fig. 1c): the NE Crater zone (NEC), Central Crater
140 zone (CC), and SW Crater zone (SWC). Effusive activity typically occurs every 5-15 years (Barberi

et al. 1993), mainly with lava flows from flank eruptive fissures spreading along the SdF (Marsella et al. 2012; Francalanci et al. 2013). The last four effusive flank eruptions occurred in 1985-86, 2002-03, 2007, and 2014, and were characterised by crater-wall collapses during the initial phases of fissure opening (De Fino et al. 1988; Calvari et al. 2005, 2010; Martini et al. 2007; Casagli et al. 2009; Giordano and Porreca 2009; Marchetti et al. 2009; Neri and Lanzafame 2009), which formed deposits that spread within the SdF depression. Although crater-wall collapses taking place at the start of flank eruptions are normally larger than the episode described here, the triggering mechanisms are the same. We therefore believe that identifying the conditions that led to the 12 January crater-wall collapse will help us improve detecting future similar events. Given the remote and dangerous position of these deposits, located along the SdF steep slope where ballistics from the summit vents fall constantly, details on their nature and emplacement conditions are scant or absent, especially for the oldest episodes. The main features of these deposits observed at Stromboli and other volcanoes are listed in Table 1.

2.3 *Previous crater-wall collapses and eruptive activity*

In 1985, a small hot rock avalanche descended the SdF slope following the opening of an eruptive fissure on the NE flank of the summit cone, but more details on this event are lacking (De Fino et al. 1988; Table 1). In 2002, a hot rock avalanche accompanied the opening of an eruptive fissure on the NE flank of the summit cone, and formed a deposit that reached the shoreline ~1.7 km away (Calvari et al. 2005; Table 1). It comprised a mixture of debris from the shattered flank of the crater, lava discharged from the crater, and loose material excavated from the SdF slope, and had an initial apparent temperature of ~368°C (Calvari et al. 2005). First-hand observations reported that when the deposit reached the shoreline, a dense ash cloud accompanied by a shower of lapilli and ash fell on the eastern flank of the SdF (Pioli et al. 2008; Table 1).

Four hours before the opening of the 2007 eruptive fissures, located again on the NE flank of the summit cone (Calvari et al. 2010), an increasing number of landslides were detected on the SdF (Martini et al. 2007). The eruption was preceded by deformation of the entire summit cone (Casaglini et al. 2009), and accompanied by a localized inflation during the opening of an effusive vent at 400 m elevation (Marchetti et al. 2009; Table 1). Then, during the effusive phase, the GPS and tilt stations recorded small but significant changes which, for the first time at this volcano, clearly indicated a deflation of the edifice in response to the magma discharge (Bonaccorso et al. 2008). The effusive flank eruption lasting from February to April 2007 (Barberi et al. 2009; Giordano and Porreca 2009; Calvari et al. 2010) caused an important structural change in the shallow feeding system of the volcano that involved an increase in intensity, frequency and volume of major explosions and summit lava overflows (Calvari et al. 2014). Between January 2007 and December 2012, the eruptive activity at Stromboli increased significantly. On average, there were 4.7 major explosions and 4.8 effusive episodes per year (Calvari et al. 2014), compared to the frequency of ~2 major explosions a year recorded before 2002 (Bertagnini et al. 1999), and to 1 effusive event every 5-15 years on average over the last 3 centuries (Barberi et al. 1993). On 24 December 2012, eruptive activity increased in intensity and caused the breaching of the NEC, followed by several overflows mainly from the NEC and powerful strombolian explosions (Calvari et al. 2014; Di Traglia et al. 2014a). This activity lasted until March 2013.

During the initial phases of the 2014 flank eruption, the rate of displacement of the volcano's summit increased (Di Traglia et al. 2015), and a new eruptive fissure opened on the NE flank of the summit cone (Rizzo et al. 2015; Table 1), followed by a growing number of landslides and hot rock avalanches along the SdF and up to the coast, ~1.7 km away. No details are available on the hot rock avalanche deposits since they were soon covered by lava flows emerging from the eruptive fissure.

3. Materials and methods

189 3.1 Webcam network

190 The observation of eruptive activity at Stromboli is carried out using the Istituto Nazionale di
191 Geofisica e Vulcanologia - Osservatorio Etneo (INGV-OE) webcam monitoring network. This
192 comprises thermal infrared ($\sim 8\text{-}14\text{ }\mu\text{m}$) and visible (400-700 nm) cameras (respectively SQT400
193 and SQV400) at 400 m elevation on the N flank of the SdF and ~ 800 m from the craters (Fig. 1b).
194 To obtain a description of the eruptive activity, the total number of explosive events each day of
195 cloud-free observation was manually counted and reported as an integer average hour value. On
196 average, 5-9% of the days were affected by clouds and/or by system failure. In such cases data are
197 lacking.

198 3.2 The GBInSAR monitoring system

199 The NE portion of the crater terrace of Stromboli (Fig. 1b-c) has been monitored since January
200 2003 (Casagli et al. 2009; Di Traglia et al. 2014b) by a GBInSAR (Ground-based synthetic aperture
201 radar interferometry) system located in a stable area outside the SdF and ~ 1.5 km from the crater
202 terrace (Fig. 1b). A GBInSAR is a remote sensing technique that uses a transmitting and a receiving
203 antenna that emits microwaves and records the amplitude and phase of the backscattered signal
204 (Rudolf et al. 1999; Luzi et al. 2004). In the configuration deployed at Stromboli, the antenna
205 moves along a 3 m-long rail (Di Traglia et al. 2014b). Working in Ku band (17.0-17.1 mm), it has
206 the advantage of penetrating dust clouds and working in any light and atmospheric condition. The
207 GBInSAR measures ground displacement in its field-of-view (FOV; Fig. 1b) along the line of sight
208 (LOS, Fig. 3a; average azimuth angle= 15°) by computing, via cross correlation, the phase
209 differences between the backscattered signals associated with two consecutive synthetic aperture
210 radar images. The phase is elaborated with interferometric techniques to retrieve the displacement
211 of the investigated area occurring between two acquisitions. Both the range and cross-range
212 resolutions are on average $2\text{ m} \times 2\text{ m}$, with a precision in displacement measurements of less than 1

213 mm. Negative and positive values of displacement indicate, respectively, a movement toward and
214 away from the sensor corresponding to either inflation (negative values) or deflation (positive
215 values) of the summit cone (Di Traglia et al. 2015). The system combines all the 8-hour averaged
216 images, “stacking” the phase of the formed interferograms (Zebker et al. 1997; Antonello et al.
217 2004; Intrieri et al. 2013; Di Traglia et al. 2014b). Interferometric stacks highlight persistent
218 deformation whereas other random signals, like atmospheric anomalies, are suppressed (Pinel et al.
219 2014). This approach is appropriate when the deformation is episodic with no change in source
220 parameters over time, as observed by Di Traglia et al. (2015) at Stromboli. The capability of SAR
221 interferometry to measure volcano deformation depends on the persistence of phase coherence over
222 the investigated time intervals (Lu et al. 2002, 2010), and also on the type of surface material,
223 which is an important factor affecting interferometric coherence (Lu et al. 2002, 2003). The loss in
224 coherence is primarily due to fast ground movements, such as the emplacement of lava flows or
225 debris avalanches (Di Traglia et al. 2013, 2014b). Here, the loss in phase coherence is used to
226 delimit the area affected by continuous erosion/deposition of material from areas influenced by
227 volcano deformation. Areas of high coherence are the external flank of the crater terrace and the
228 SdF (Fig. 2), whereas the NEC talus (Fig. 1c) shows very low coherence even at short-interval
229 interferograms (< 1 day). Moreover, for interferometric analysis a coherence threshold equal to or
230 above 0.8 is required to consider the information on the deformation reliable (Di Traglia et al.
231 2014b). The GBInSAR time series extracted in this study derives from an area located on the
232 external part of the crater terrace characterised by high-coherence (Fig. 3a, left inset), whose
233 measurements over time have displayed the best consistency and accuracy (Di Traglia et al. 2014c,
234 2015).

235 Backscattered intensity of each image, derived from real (i) and imaginary (q) parts of the complex
236 SAR data was transformed in amplitude image and then decibel scaled, converting the data with a
237 virtual band with the equation $10 \times \log_{10}(\text{Amplitude})$. The amplitude is proportional to the energy
238 reflected by the targets and depends on characteristics such as dielectric properties of the reflecting

239 materials, their orientation with respect to the receiving antenna (which in turn is related to the
240 smoothness or roughness of the surface) and meteorological conditions. From amplitude squared it
241 is possible to produce power images. They are useful to observe and quantify geomorphological
242 changes of a topographic surface (Wadge and Haynes 1998; Macfarlane et al. 2006; Wadge et al.
243 2002, 2008, 2011, 2014), such as, for the case of Stromboli, formation and changes of the NEC
244 notch or growth of NEC talus (Di Traglia et al. 2014a). In order to quantitatively evaluate the
245 changes in the NEC's morphology, daily-averaged power images produced by the GBInSAR were
246 used. The system produces an image every 11 minutes, therefore ~130 of them are used to form an
247 averaged one to make a day. This process increases the signal to noise ratio and therefore facilitates
248 the interpretation. Since the NEC rim produces a shadow zone corresponding to the crater
249 depression, it is possible to calculate the area of the crater itself as it changes over time (Fig. 3a).
250 The precision of the measurements is affected by pixels size (increasing with distance) and by the
251 amplitude of the backscattered signals, which is not constant with time, thus causing uncertainty
252 when determining the boundary of the crater area. When the areal extent of the crater depression
253 can be assumed stable (that is during periods of low volcanic activity) it is possible to calculate the
254 precision (standard deviation) of such method. For this application the standard deviation has been
255 calculated equal to 80 m². To map the area affected by the 12 January crater-wall collapse, a
256 threshold was set at ~55 dB.

257 The background topographic data are represented by a very high resolution Digital Elevation Model
258 (DEM) with a spatial resolution of 50 cm provided by the Italian Department of Civil Protection
259 (DPC) to University of Florence. This DEM was obtained elaborating the 3D data (8 pt/m²)
260 acquired during the airborne laser scanning survey carried out from 4 to 18 May 2012 by BLOM
261 Compagnia Generale Riprese aeree S.P.A. (www.blomasa.com). The data were acquired using the
262 Leica ADS80 sensor, whose instrumental vertical and horizontal accuracy is $\pm 10/20$ cm and ± 25
263 cm, respectively. The map was generated using an ESRI platform.

264 4. Results

265 Several lava overflows occurred between 7 and 16 January 2013, spreading down the SdF slope, as
266 detected from the webcam monitoring system. At this time, the NEC zone comprised two main
267 cones and a hornito (NEC1, NEC2 and NEC hornito, Figs. 1c, 3a) on the crater rim, whose
268 powerful strombolian activity caused both their fast growth as well as frequent fallout of bombs on
269 the upper SdF, thus increasing the volume of a wide and thick talus (NEC talus, Figs. 1c, 3a, 4a)
270 formed after the 2007 eruption on the N outer flank of the crater area.

271 Early on 11 January 2013, two small lava flows emerged from two vents at the base of the NEC
272 (Fig. 4b). At this stage, lava was intruding through the crater wall, largely formed of spatter
273 agglutinate and minor lapilli. Explosive activity increased during the day together with spattering
274 from the NEC hornito. At ~23:40 (all times are UT), a ~15 m wide lava flow erupted from a saddle
275 between the NEC hornito and NEC2 (Figs. 4c-d), and began to spread northward along the NEC
276 talus. At 05:44 on 12 January, powerful ~150 m high explosions occurred within the crater (Fig.
277 4e). At ~11:14, there was the sudden failure of the NEC wall, forming an extensive, vertically
278 rising, brown dust cloud. The strong wind drove the ash cloud rapidly upwards and southwards, and
279 heavy ash fall was reported along the margins of the SdF and in the eastern sector of the island,
280 reaching Stromboli village (Di Traglia et al. 2014a) and dissipating in the following hour.

281 Based on the images recorded by the visible and thermal webcams, we estimated that the maximum
282 height of the collapsed crater wall, referred to here as the vertical elevation lost by the crater rim,
283 was ~20-30 m (Figs. 4f-g). Power images allowed estimating that ~2400 m² were involved in the
284 collapse and therefore the volume of rocks falling during the crater-wall failure was ~10⁵ m³.

285 After the NEC failure, a significant effusive event took place between 13 and 16 January, with a ~5
286 m thick lava overflowing from the saddle between NEC1 and NEC2 and forming 3-4 lava branches
287 along the SdF. This saddle was wider and deeper than before (Fig. 4g) because of the removal of the

288 crater rim following the 12 January crater-wall collapse, and the lava flow eventually drained the
289 magma from the crater depression. Several lava flows erupted again between 8 and 18 February and
290 between 27 February and 2 March from the NEC saddle, forming several lava branches on the
291 upper SdF.

292 The 2012-13 activity was accompanied by a long-term inflation of the summit vents area as
293 detected from GBInSAR (Fig. 3b), with an estimated accumulated magma volume in the period 8
294 August 2012 - 8 March 2013 of $\sim 9.61 \pm 5.34 \times 10^4 \text{ m}^3$ and an average accumulation rate of
295 $\sim 5.25 \pm 2.92 \times 10^{-3} \text{ m}^3 \text{ s}^{-1}$ (Di Traglia et al. 2015).

296 Figure 5 shows a comparison between the trend of explosive activity obtained from the webcam
297 monitoring network (Fig. 5a), the inflation-deflation of the summit cone as revealed by the
298 displacements recorded by the GBInSAR (Fig. 5b), and the crater area obtained from GBInSAR
299 power images (Fig. 5c). Several lava overflows from the summit cone occurred in December 2012
300 and January 2013 (red triangles in Fig. 5). During the period of no lava emission, the NEC produced
301 intense spattering. Effusive activity happened again on 11–27 February 2013, with overflows and
302 intense spattering activity from the NEC (Calvari et al. 2014; Di Traglia et al. 2014a).

303 The period considered here (8 December 2012 - 8 March 2013, Fig. 5) can be divided into five
304 phases. The first phase, from 8 to 27 December 2012, corresponded to a great variability in the
305 number of explosions from the summit vents (3-16 explosions/hour, Fig. 5a), and to a short-term
306 inflation of the summit cone (Fig. 5b). The crater area was roughly constant ($\sim 700 \text{ m}^2$) until 13
307 December 2012 (Fig. 5c, grey arrow indicating crater widening), when it began to increase almost
308 regularly up to 1670 m^2 on 6 January 2013, six days before the crater-wall collapse. The second
309 phase, lasting from 27 December 2012 to 12 January 2013, displayed a marked and regular increase
310 in explosive activity (from 3 to 13 explosions/hour, Fig. 5a) interrupted by jumps associated with
311 lava overflows from the summit (red triangles in Fig. 5). A short-term deflation occurred between

the end of the first and the start of the second phase, caused by several lava flows (Fig. 5b). The second phase was characterised by a faster but more variable crater area widening (Fig. 5c, grey arrow indicating fast crater widening), and on 7 January 2013 the crater underwent an enlargement toward the talus at its base, reaching an area of $\sim 2380 \text{ m}^2$ (Fig. 5c). This second phase culminated with the 11-12 January lava flows and with the 12 January crater-wall collapse (Fig. 5). After the crater-wall collapse and until 15 January (third phase), there was a remarkable variability in the explosive rate (Fig. 5a), a rapid deflation of the summit cone (Fig. 5b) as well as a faster widening of the crater area (Fig. 5c) that culminated with a maximum of 2870 m^2 recorded on 15 January. This was a consequence of the significant lava flow output lasting between 13 and 16 January that drained the uppermost conduit, causing a sudden variability in explosive activity and an erosion of the crater. The fourth phase displayed a highly variable explosive rate (5-14 explosions/hour, Fig. 5a), an initial short-term deflation of the summit cone (Fig. 5b), and a faster crater area narrowing (Fig. 5c) until 21 January. The much longer fifth phase lasted until 3 March and showed slight oscillations but almost stable values of all parameters, with several small lava overflows from the summit cone between 8 and 18 February (Fig. 5), and the recovery of the deflation of the summit cone on 15 February (Fig. 5b), when the lava flow output almost ended but the explosive activity was still high. A gradual shrinking of the NEC crater area started from 18 January (Fig. 5c), with the formation of a lower crater rim. No further crater-wall collapse events occurred during this stage.

5. Discussion and concluding remarks

Combining the results of this work with previously published data, a model linking shallow magma accumulation and migration beneath the vents, eruptive activity, and slope instability is presented. Di Traglia et al. (2015) indicated the presence of a shallow magma storage at $\sim 482 \pm 46 \text{ m a.s.l.}$ ($268 \pm 46 \text{ m}$ beneath the crater terrace). Changes in the magma rise and accumulation rate at shallow level at persistently erupting volcanoes are common, and are generally related to the

337 reservoir pressure and the density contrast between magma and host rocks (Coppola et al. 2012;
338 Bagnardi et al. 2014; Patrick et al. 2015). At Stromboli, evidence of deep supply was detected at the
339 end of 2009, and perhaps also at the end of 2008, by peaks of fumarole temperature, and CO₂ and
340 SO₂ signals, as reported by Calvari et al. (2014). Magma accumulation within the shallow storage
341 zone at Stromboli produced inflation of the crater terrace, with periods (2-3 months) of higher
342 displacement rate recorded by the GBInSAR, coherent with higher-magma accumulation rate (Di
343 Traglia et al. 2015). These phases of high accumulation rate are also testified to by the fluctuations
344 of radiative power detected by MODIS (Moderate Resolution Imaging Spectroradiometer; Coppola
345 et al. 2012) and eruptive activity (Calvari et al. 2014). On the other hand, short-term variations
346 (hours to days) in the displacement rate were well correlated with changes in seismic tremor,
347 allowing Di Traglia et al. (2014c) to determine that the coupling between the deformation of the
348 crater terrace with tremor amplitude is related to the variation in magma level within the uppermost
349 part of the conduit. This in turn is related to increasing magma vesiculation (i.e. decreasing magma
350 density), which implies enhanced degassing activity. Di Traglia et al. (2014c) also showed that both
351 the ground deformation and serial increase in tremor amplitude happen before (between 2 and 6
352 days) the series of very-long-period (VLP) seismic signals. The increasing rate of overall volume
353 change associated with VLP signals before inflation implies that slug formation, release and burst
354 (identified by the VLPs) precede the steady state bulk transfer of outgassed volatiles.

355 Using an integrated monitoring network comprising visible and thermal webcams as well as
356 GBInSAR, this paper goes beyond this model, identifying the relationship between the volcano
357 behaviour and associated small-scale (type 3 landslide) slope instability phenomena. Although the
358 size of the 12 January 2013 event was smaller than the failures accompanying the start of flank
359 eruptions (Casagli et al. 2009; Marchetti et al. 2009), our data suggest that the processes triggering
360 it were very similar. On the basis of the analysed data, we propose a sequence of events that led to
361 crater-wall collapse. The 12 January 2013 crater-wall collapse event occurred in a period of long-

term inflation of the summit area (Fig. 3b), and was preceded by an increasing level of explosive activity at the summit vents (Fig. 5a, second phase), associated with oscillating daily displacement (Fig. 5b), and with widening of the crater area (Fig. 5c). All the data presented here point to a sequence of events that, when combined, led to crater-wall instability and collapse.

5.1 Rapid crater growth and weakness

The NEC portion of the summit cone at Stromboli built up very quickly over a period of months as a consequence of powerful explosive activity that led to greater deposition of scoria and cinders. The crater wall was very weak, however, being essentially made of loose spatter and smaller amounts of ash (Fig. 4g). During each NEC explosion, high temperature points were observed expanding through the vents opened on the NE rim of the NEC (Fig. 4c), which allowed us to recognize that the crater wall was already fractured at its base and thus prone to fail at several points. These vents erupted small lava lobes (Fig. 4b), further eroding the crater wall at several points and indicating that the ~20-30 m uppermost portion of the NEC was extensively fractured before the 12 January crater-wall collapse. This is comparable to similar episodes described at other volcanoes, such as Etna, Montserrat, and Chaîne Des Puys (Guest et al. 1974; Calvari and Pinkerton 2002; Sparks et al. 2002; Voight et al. 2002; Behncke et al. 2003, 2008; Petronis et al. 2013).

5.2 Increasing magma level

The 12 January 2013 crater-wall collapse occurred during a period characterised by an increasing average number of explosions per hour and inflation of the summit cone (Figs. 5a and 3b). Calvari et al. (2005, 2010), Burton et al. (2008). Ripepe et al. (2009) have argued that the number of explosions per hour is an indirect measure of magma input rate and magma level within the conduit, where an increasing magma level may be associated with more violent and frequent explosive activity. Casagli et al. (2009) and Di Traglia et al. (2014b, 2015) have shown that GBInSAR at Stromboli recorded inflation before the opening of effusive vents, also confirmed by tiltmeters

386 (Marchetti et al. 2009). Thus, a period characterised by greater explosive activity and inflation of
387 the summit cone corresponds to an increasing magma level within the conduit and hence also to a
388 higher magmastatic pressure, this being the pressure exerted by the magma filling in the conduit
389 (Elsworth and Day 1999; Melnik and Sparks 2002; Battaglia et al. 2011; Di Traglia et al. 2014b;
390 Patrick et al. 2015). This condition implies that more accumulated energy has become available to
391 the system to fracture the summit cone (Di Traglia et al. 2015). The initiation and propagation of a
392 fracture depend on the potential energy stored in a volcanic edifice when it is loaded (Gudmundsson
393 2009, 2012), which is primarily related to inflation of the shallow magma storage area (Browning et
394 al. 2015; Di Traglia et al. 2015). High magma levels within the conduit also accompanied crater-
395 wall collapse at Arenal and Montserrat, even in the absence of explosive activity (Alvarado and
396 Soto 2002; Sparks et al. 2002; Voight et al. 2002; Cole et al. 2005). The cyclic stresses represented
397 by magmastatic pressure variation and frequent explosions also had the effect of weakening the
398 crater wall, because they caused fatigue and therefore reduced strength of the rock mass so that it
399 could fail at a lower stress (Erarslan and Williams 2015).

400 *5.3 Lava flows and causes of crater-wall collapse*

401 A third cause of the failure was the emission of lava flows, from early 11 January 2013, thus ~1.5
402 days before the failure and where the failure occurred, from vents located ~20-30 meters below the
403 NEC rim. This was accompanied by strong explosive activity that continued within the crater (Figs.
404 4b-e), and indicates that the magma level within the conduit remained high and near the crater rim,
405 as observed in Figure 3b-e and confirmed by direct observations. Magma fingering at the base of
406 cinder cones has been recognised by geological studies as a cause of crater-wall failure, causing
407 weakening and formation of failure planes (Houghton and Schmincke 1989; Baer 1991; Sparks et
408 al. 2002; Voight et al. 2002; Petronis et al. 2013; Geshi and Neri 2014).

409 All these processes further diminished the integrity of the crater wall and triggered the failure of
410 $\sim 10^5 \text{ m}^3$ rock. Following the collapse event, there was rapid reconstruction of the crater wall when
411 coarse spatter accumulated on the crater rim during intense explosions that characterized the 16-18
412 January interval, also demonstrated by direct observation (Di Traglia et al. 2014a). These
413 observations are a valuable demonstration of how a changing magmatic system can destabilize
414 portions of an edifice, with hazardous results.

415 A few hours before the collapse, landslides started to occur on the NE flank of the NEC with
416 increasing frequency until the failure of the NEC wall. The 12 January 2013 crater-wall collapse
417 took place during a long-term inflation of the summit cone (Fig. 3b) and marked the transition
418 between a short-term inflation and a short-term deflation of the summit cone (Fig. 5b). The short-
419 term deflation reached its climax on 15 January 2013 (Fig. 5b), concomitant with emptying of the
420 summit portion of the volcano due to the 13-15 January 2013 overflows. Following these
421 overflows, inflation occurred again at a higher rate than before (Fig. 5b), causing high variability in
422 the average number of explosions per hour (Fig. 5a), but no further crater-wall collapse.

423 After this, even though the daily average number of explosions remained at pre-12 January
424 frequency (Fig. 5a), they did not produce the same destructive effects as before on the crater wall.
425 This was because deposition of new material, of greater strength, produced more-robust crater
426 walls; there was also an absence of simultaneous short-term inflation (Fig. 5b), and thus an absence
427 of high magmastatic pressure within the conduit. Edifice stressing due to short-term inflation and
428 powerful explosive activity significantly reduces the static elastic moduli of volcanic rocks, while
429 healing and consolidation can account for the renewal of strength of the volcanic edifice (Heap et
430 al. 2009, 2011; Carrier et al. 2015).

431 These data all suggest that the crater-wall collapse described here was closely related to the
432 simultaneous occurrence of several things; there was: 1) weakness of the summit cone, 2)

433 increasing explosion rate and short-term inflation of the summit cone, with these last two both
434 indicating high magmastatic pressure within the conduit, and 3) weakening of the cone by magma
435 fingering. The combination of these things therefore represents a critical condition for potential
436 triggering of a crater-wall failure that evolves into landslides or hot avalanches along the SdF.

437 *5.4 The 12 January crater-wall collapse in the context of previous failures at Stromboli*

438 Since 1985, all flank eruptions at Stromboli have been heralded by the collapse of a portion of the
439 summit cone, causing landslides or hot avalanches along the SdF (De Fino et al. 1988; Calvari et al.
440 2005, 2010; Martini et al. 2007; Giordano and Porreca 2009; Neri and Lanzafame 2009; Ripepe et
441 al. 2009). Although the 12 January 2013 event is smaller than the failures accompanying the start of
442 flank eruptions, the processes that triggered it are substantially similar to those occurring at the start
443 of flank eruptions. As an example, before the 7 August 2014 flank eruption at Stromboli, several
444 crater-wall collapses took place, with an increase in magnitude and frequency with time. This
445 happened together with a major inflation of the system, testifying to the considerable accumulation
446 of magma ($1.24 \pm 6.88 \times 10^{-2} \text{ m}^3 \text{ s}^{-1}$) at very shallow level.

447 The combination of factors identified in this work could be a general mechanism for the generation
448 of crater-wall collapses, also applicable to other and more dangerous volcanoes, such as Arenal
449 Volcano in Costa Rica (Alvarado and Soto 2001; Cole et al. 2005), El Misti in Peru (Cobenas et al.
450 2012), Merapi in Indonesia (Gertisser et al. 2011), Colima in Mexico (Savov et al. 2008), Mt. Etna
451 in Italy (Calvari and Pinkerton 2002; Behncke et al. 2003, 2008), or Soufrière Hills on Montserrat
452 (Sparks et al. 2002; Voight et al. 2002). These observations are a valuable demonstration of how
453 changes to a magmatic system can destabilize portions of the edifice, with hazardous results.
454 Tracking of such changes has proven a valid tool for forecasting the occurrence of failures, and
455 could possibly be applied to other volcanoes.

457 **Acknowledgments**

458 The National Civil Protection Department (DPC) is acknowledged for supporting the project and
459 enabling this publication. The authors are grateful to D. Mangione (DPC) for permission to use and
460 publish his photos, to the GBInSAR monitoring group of the Department of Earth Sciences -
461 University of Firenze (UNIFI); to E. Biale, E. Pecora and M. Prestifilippo for the installation and
462 maintenance of the INGV-OE webcam network; and to four anonymous reviewers for their
463 comments on an earlier version of this manuscript. Stephen Conway improved the English style.
464 The GBInSAR apparatus used in this application was designed and produced by the Ellegi s.r.l. and
465 based on the proprietary technology GBInSAR LiSALAB derived from the evolution and
466 improvement of LiSA technology licensed by the Ispra Joint Research Centre of the European
467 Commission. The Digital Elevation Model (DEM) with a spatial resolution of 50 cm was provided
468 by the Italian Department of Civil Protection (DPC) to University of Florence in the framework of
469 the research agreements SAR.net, SAR.net2, InGrID and InGrID2015 projects.

470 The cumulative displacement map and time-series were produced by the LiSA (Linear SAR) system
471 developed by Ellegi LLC using proprietary GBInSAR technology by LiSALab LLC, a European
472 Commission Joint Research Centre spin-off, and installed at Stromboli by UNIFI (owner of the
473 system), in the framework of research agreements (SAR.net, SAR.net2, InGrID and InGrID2015
474 projects) with the Presidenza del Consiglio dei Ministri – DPC.

475

476 **References**

477 Acocella V (2005) Modes of sector collapse of volcanic cones: Insights from analogue experiments.
478 J Geophys Res 110 (B02205). doi:10.1029/2004JB003166

479 Acocella V, Neri M (2009) Dike propagation in volcanic edifices: Overview and possible
 480 developments. *Tectonophysics* 471:67–77

481 Alvarado GE, Soto GJ (2002) Pyroclastic flow generated by crater-wall collapse and outpouring of
 482 the lava pool of Arenal Volcano, Costa Rica. *Bull Volcanol* 63(8):557-568. doi: 10.1007/s00445-
 483 001-0179-9

484 Andronico D, Corsaro RA, Cristaldi A, Polacci M (2008) Characterizing high energy explosive
 485 eruptions at Stromboli volcano using multidisciplinary data: An example from the 9 January 2005
 486 explosion. *J Volcanol Geotherm Res* 176:541-550

487 Antonello G, Casagli N, Farina P, Leva D, Nico G, Sieber AJ, Tarchi D (2004) Ground-based SAR
 488 interferometry for monitoring mass movements. *Landslides* 1(1):21-28

489 Baer G (1991) Mechanisms of Dike Propagation in Layered Rocks and in Massive, Porous
 490 Sedimentary Rocks. *J Geophys Res* 96(B7):11,911-11,929

491 Bagnardi M, Poland MP, Carbone D, Baker S, Battaglia M, Amelung F (2014) Gravity changes and
 492 deformation at Kīlauea Volcano, Hawaii, associated with summit eruptive activity, 2009–2012. *J*
 493 *Geophys Res-Sol EA* 119(9):7288-7305

494 Barberi F, Rosi M, Sodi A (1993) Volcanic hazard assessment at Stromboli based on review of
 495 historical data. *Acta Vulcanol* 3:173-187

496 Barberi F, Civetta L, Rosi M, Scandone R (2009) Chronology of the 2007 eruption of Stromboli
 497 and the activity of the Scientific Synthesis Group. *J Volcanol Geotherm Res* 182:123-130. doi:
 498 10.1016/j.jvolgeores.2008.09.019

499 Battaglia M, Di Bari M, Acocella V, Neri M (2011) Dike emplacement and flank instability at
 500 Mount Etna: Constraints from a poro-elastic-model of flank collapse. *J Volcanol Geotherm Res*
 501 199:153-164. doi: 10.1016/j.jvolgeores.2010.11.005

502 Behncke B, Neri M, Carniel R (2003) An exceptional case of lava dome growth spawning
 503 pyroclastic avalanches at Mt. Etna (Italy): the 1999 Bocca Nuova eruption. *J Volcanol Geotherm*
 504 *Res* 124:115-128

505 Behncke B, Calvari S, Giammanco S, Neri M, Pinkerton H (2008) Pyroclastic density currents
 506 resulting from the interaction of basaltic magma with hydrothermally altered rock: an example from
 507 the 2006 summit eruptions of Mount Etna, Italy. *Bull Volcanol* 70(10):1249-1268

508 Bertagnini A, Coltelli M, Landi P, Pompilio M, Rosi M (1999) Violent explosions yield new
 509 insights into dynamics of Stromboli volcano. *Eos AGU Transactions* 80(52):633-636

510 Bertolaso G, Bonaccorso A, Boschi E (2008) Scientific Community and Civil Protection Synergy
 511 During the Stromboli 2002-2003 Eruption. In: Calvari S, Inguaggiato S, Puglisi G, Ripepe M, Rosi
 512 M (eds) *The Stromboli Volcano: an integrated study of the 2002–2003 eruption*. AGU Geophys
 513 *Monogr Ser* 182:387–397. doi:10.1029/182GM31

514 Billi A, Acocella V, Funicello R, Giordano G, Lanzafame G, Neri M (2003) Mechanisms for
 515 ground-surface fracturing and incipient slope failure associated with the 2001 eruption of Mt. Etna,
 516 Italy: analysis of ephemeral field data. *J Volcanol Geotherm Res* 122:281-294

517 Bonaccorso A, Calvari S, Linde A, Sacks S, Boschi E (2012) Dynamics of the shallow plumbing
 518 system investigated from borehole strainmeters and cameras during the 15 March, 2007 Vulcanian
 519 paroxysm at Stromboli volcano. *Earth Plan Sci Lett* 357-358:249-256

520 Bonaccorso A, Gambino S, Guglielmino F, Mattia M, Puglisi G, Boschi E (2008) Stromboli 2007
 521 eruption: Deflation modeling to infer shallow-intermediate plumbing system. *Geophys Res Lett* 35:
 522 L06311. doi:10.1029/2007GL032921

523 Bonforte A, Guglielmino F (2015) Very shallow dyke intrusion and potential slope failure imaged
 524 by ground deformation: The 28 December 2014 eruption on Mount Etna. *Geophys Res Lett* 42.
 525 doi:10.1002/2015GL063462

526 Browning J, Drymoni K, Gudmundsson A (2015). Forecasting magma-chamber rupture at Santorini
 527 volcano, Greece. *Scientific reports* 5:15785. doi:10.1038/srep15785

528 Burton MR, Calvari S, Spampinato L, Lodato L, Pino NA, Marchetti E, Murè F (2008) Volcanic
 529 and seismic activity at Stromboli preceding the 2002–2003 eruption. In: Calvari S, Inguaggiato S,
 530 Puglisi G, Ripepe M, Rosi M (eds) *The Stromboli Volcano: an integrated study of the 2002–2003*
 531 *eruption*. AGU Geophys Monogr Ser 182:93–104. doi:10.1029/182GM09

532 Calvari S, Bonaccorso A, Madonia P, Neri M, Liuzzo M, Salerno GG, Behncke B, Caltabiano T,
 533 Cristaldi A, Giuffrida G, La Spina A, Marotta E, Ricci T, Spampinato L (2014) Major eruptive style
 534 changes induced by structural modifications of a shallow conduit system: the 2007-2012 Stromboli
 535 case. *Bull Volcanol* 76:841. doi:10.1007/s00445-014-0841-7

536 Calvari S, Buttner R, Cristaldi A, Dellino P, Giudicepietro F, Orazi M, Peluso R, Spampinato L,
 537 Zimanowski B, Boschi E (2012) The 7 September 2008 Vulcanian explosion at Stromboli volcano:
 538 Multiparametric characterization of the event and quantification of the ejecta. *J Geophys Res* 117
 539 (B05201). doi:10.1029/2011JB009048

540 Calvari S, Lodato L, Steffke A, Cristaldi A, Harris AJL, Spampinato L, Boschi E (2010) The 2007
 541 Stromboli eruption: event chronology and effusion rates using thermal infrared data. *J Geophys Res*
 542 115 (B04201). doi:10.1029/2009JB006478

543 Calvari S, Pinkerton H (2002) Instabilities in the summit region of Mount Etna during the 1999
544 eruption. *Bull Volcanol* 63:526-535

545 Calvari S, Pinkerton H (2004) Birth, growth and morphologic evolution of the "Laghetto" cinder
546 cone during the 2001 Etna eruption. *J Volcanol Geotherm Res* 132:225-239. doi:10.1016/S0377-
547 0273(03)00347-0

548 Calvari S, Spampinato L, Lodato L, Harris AJL, Patrick MR, Dehn J, Burton MR, Andronico D
549 (2005) Chronology and complex volcanic processes during the 2002-2003 flank eruption at
550 Stromboli volcano (Italy) reconstructed from direct observations and surveys with a handheld
551 thermal camera. *J Geophys Res* 110 (B02201). doi:10.1029/2004JB003129

552 Calvari S, Spampinato L, Lodato L (2006) The 5 April 2003 vulcanian paroxysmal explosion at
553 Stromboli volcano (Italy) from field observations and thermal data. *J Volcanol Geotherm Res*
554 149(1):160-175

555 Carrier A, Got JL, Peltier A, Ferrazzini V, Staudacher T, Kowalski P, Boissier P (2015) A damage
556 model for volcanic edifices: Implications for edifice strength, magma pressure, and eruptive
557 processes. *J Geophys Res* 120(1):567-583

558 Casagli N, Tibaldi A, Merri A, Del Ventisette C, Apuani T, Guerri L, Fortuny-Guasch J, Tarchi D
559 (2009) Deformation of Stromboli Volcano (Italy) during the 2007 eruption revealed by radar
560 interferometry, numerical modelling and structural geological field data. *J Volcanol Geotherm Res*
561 182:182-200

562 Charbonnier SJ, Gertisser R (2009) Numerical simulations of block-and-ash flows using the
563 Titan2D flow model: examples from the 2006 eruption of Merapi Volcano, Java, Indonesia. *Bull*
564 *Volcanol* 71(8):953-959

565 Chouet B, Hamisevicz N, McGetchin TR (1974) Photoballistics of Volcanic Jet Activity at
 566 Stromboli, Italy. *J Geophys Res* 79(32):4961-4976

567 Cigolini C, Laiolo M, Coppola D (2014) Revisiting the last major eruptions at Stromboli volcano:
 568 inferences on the role of volatiles during magma storage and decompression. In: Zellmer GF,
 569 Edmonds M, Straub SM (eds), *The Role of Volatiles in the Genesis, Evolution and Eruption of Arc*
 570 *Magmas*. Geol Soc London Special Publ 410:33-70

571 Cobeñas G, Thouret J-C, Bonadonna C, Boivin P (2012) The c.2030 yr BP Plinian eruption of El
 572 Misti volcano, Peru: Eruption dynamics and hazard implications. *J Volcanol Geotherm Res* 241-
 573 242:105-120. doi:10.1016/j.jvolgeores.2012.06.006

574 Cole PD, Calder ES, Druitt TH, Hoblitt RP, Robertson R, Sparks RSJ, Young SR (1998)
 575 Pyroclastic flow generated by gravitational instability of the 1996-97 lava dome of Soufriere Hills
 576 Volcano, Montserrat. *Geophys Res Lett* 25(18):3425-3428

577 Cole PD, Calder ES, Sparks RSJ, Clarke A, Druitt TH, Young SR, Herd R, Harford CL, Norton G
 578 (2002) Deposits from dome-collapse and fountain-collapse pyroclastic flows at Soufrière Hills
 579 Volcano, Montserrat. In: Druitt TH and Kokelaar BP (eds) *The Eruption of Soufrière Hills Volcano,*
 580 *Montserrat, from 1995 to 1999*. Geol Soc London Mem 21: 231-262

581 Cole PD, Fernandez E, Duarte E, Duncan AM (2005) Explosive activity and generation
 582 mechanisms of pyroclastic flows at Arenal volcano, Costa Rica between 1987 and 2001. *Bull*
 583 *Volcanol* 67(8):695-716

584 Cole PD, Scarpati C (2010) The 1944 eruption of Vesuvius, Italy: combining contemporary
 585 accounts and field studies for a new volcanological reconstruction. *Geol Mag* 147(3):391-415.
 586 doi:10.1017/S0016756809990495

587 Coppola D, Piscopo D, Laiolo M, Cigolini C, Delle Donne D, Ripepe M (2012) Radiative heat
588 power at Stromboli volcano during 2000–2011: Twelve years of MODIS observations. *J Volcanol*
589 *Geotherm Res* 215-216:48-60. doi: 10.1016/j.jvolgeores.2011.12.001

590 De Fino M, La Volpe L, Falsaperla S, Frazzetta G, Neri G, Francalanci L, Rosi M, Sbrana A (1988)
591 The Stromboli eruption of December 6, 1985 - April 25, 1986: volcanological, petrological and
592 seismological data. *Rend Soc It Min Petr* 43:1021-1038

593 Di Traglia F, Battaglia M, Nolesini T, Lagomarsino D, Casagli N (2015) Shifts in the eruptive
594 styles at Stromboli in 2010–2014 revealed by ground-based InSAR data. *Scientific Reports*
595 5:13569. doi:10.1038/srep13569

596 Di Traglia F, Cauchie L, Casagli N, Saccorotti G (2014c) Decrypting geophysical signals at
597 Stromboli Volcano (Italy): Integration of seismic and Ground-Based InSAR displacement data.
598 *Geophys Res Lett* 41:2753-2761

599 Di Traglia F, Intrieri E, Nolesini T, Bardi F, Del Ventisette C, Ferrigno F, Frangioni S, Frodella W,
600 Gigli G, Lotti A, Tacconi Stefanelli C, Tanteri L, Leva D, Casagli N (2014a) The Ground-Based
601 InSAR monitoring system at Stromboli volcano: linking changes in displacement rate and intensity
602 of persistent volcanic activity. *Bull Volcanol* 76(2):1-18

603 Di Traglia F, Nolesini T, Intrieri E, Mugnai F, Leva D, Rosi M, Casagli N (2014b) Review of ten
604 years of volcano deformations recorded by the ground-based InSAR monitoring system at
605 Stromboli volcano: a tool to mitigate volcano flank dynamics and intense volcanic activity. *Earth*
606 *Science Reviews* 139:317-335

607 Di Traglia F, Ventisette C, Rosi M, Mugnai F, Intrieri E, Moretti S, Casagli N (2013) Ground-based
608 InSAR reveals conduit pressurization pulses at Stromboli volcano. *Terra Nova* 25(3):192-198

609 Elsworth D, Day SJ (1999) Flank collapse triggered by intrusion: the Canarian and Cape Verde
610 Archipelagoes. *J Volcanol Geotherm Res* 94:323-340

611 Erarslan N, Williams DJ (2015) The damage mechanism of rock fatigue and its relationship to the
612 fracture toughness of rocks. *Int J Rock Mech Min Sci* 56:15-26

613 Eychenne J, Le Pennec J-L, Ramon P, Yepes H (2013) Dynamics of explosive paroxysms at open-
614 vent andesitic systems: High-resolution mass distribution analyses of the 2006 Tungurahua fall
615 deposit (Ecuador). *Earth Plan Sci Letters* 361:343-355. <http://dx.doi.org/10.1016/j.epsl.2012.11.002>

616 Francalanci L, Lucchi F, De Astis G, Tranne CA (2013) Eruptive, volcano-tectonic and magmatic
617 history of the Stromboli volcano (north-eastern Aeolian archipelago). In: Lucchi F, Peccerillo A,
618 Keller J, Tranne CA, Rossi PL (eds) *The Aeolian Islands Volcanoes*. *Geol Soc London Memoirs*
619 37:397-471. <http://dx.doi.org/10.1144/M37.13>

620 Gaudin D, Moroni M, Taddeucci J, Scarlato P, Shindler L (2014) Pyroclast Tracking Velocimetry:
621 A particle tracking velocimetry-based tool for the study of Strombolian explosive eruptions. *J*
622 *Geophys Res* 119:5369-5383. doi:10.1002/2014JB011096

623 Gertisser R, Charbonnier SJ, Troll VR, Keller J, Preece K, Chadwick JP, Barclay J, Herd RA
624 (2011) Merapi (Java, Indonesia): anatomy of a killer volcano. *Geol Today* 27:57-62

625 Geshi N, Neri M (2014) Dynamic feeder dyke systems in basaltic volcanoes: the exceptional
626 example of the 1809 Etna eruption (Italy). *Frontiers in Earth Science* 2(13):1-11. doi:
627 10.3389/feart.2014.00013

628 Giordano G, Porreca M (2009) Field observations on the initial lava flow and the fracture system
629 developed during the early days of the Stromboli 2007 eruption. *J Volcanol Geotherm Res* 182:145-
630 154

631 Gudmundsson A (2009) Toughness and failure of volcanic edifices. *Tectonophysics* 471:7-35.
632 doi:10.1016/j.tecto.2009.03.001

633 Gudmundsson A (2012) Strengths and strain energies of volcanic edifices: implications for
634 eruptions, collapse calderas, and landslides. *Nat Hazards Earth Syst Sci* 12:2241-2258.
635 doi:10.5194/nhess-12-2241-201

636 Guest JE, Huntingdon AT, Wadge G, Brander JL, Booth B, Carter S, Duncan A (1974) Recent
637 Eruption of Mount Etna. *Nature* 250:385-387

638 Harris A (2013) *Thermal Remote Sensing of Active Volcanoes: A User's manual*. Cambridge
639 University Press 728 pp, ISBN 978-0-521-85945-5

640 Harris AJL, Ripepe M, Calvari S, Lodato L, Spampinato L (2008) The 5 April 2003 Explosion of
641 Stromboli: Timing of Eruption Dynamics using Thermal Data. In: Calvari S, Inguaggiato S, Puglisi
642 G, Ripepe M, Rosi M (eds) *The Stromboli Volcano: an integrated study of the 2002–2003 eruption*.
643 AGU Geophys Monogr Ser 182:305-316. doi: 101029/182GM25

644 Hazlett RW, Buesch D, Anderson JL, Elan R, Scandone R (1991) Geology, failure conditions, and
645 implications of seismogenic avalanches of the 1944 eruption at Vesuvius, Italy. *J Volcanol*
646 *Geotherm Res* 47:249-264

647 Heap MJ, Baud P, Meredith PG, Vinciguerra S, Bell AF, Main IG (2011) Brittle creep in basalt and
648 its application to time-dependent volcano deformation. *Earth Plan Sci Lett* 307(1):71-82

649 Heap MJ, Vinciguerra S, Meredith PG (2009) The evolution of elastic moduli with increasing crack
650 damage during cyclic stressing of a basalt from Mt. Etna volcano. *Tectonophysics* 471:153-160

651 Houghton BF, Schmincke H-U (1989) Rothenberg scoria cone, East Eifel: a complex Strombolian
652 and phreatomagmatic volcano. *Bull Volcanol* 52:28-48

653 Intrieri E, Di Traglia F, Del Ventisette C, Gigli G, Mugnai F, Luzi G, Casagli N (2013) Flank
 654 instability of Stromboli volcano (Aeolian Islands, Southern Italy): integration of GB-InSAR and
 655 geomorphological observations. *Geomorphology* 201:60-69

656 Leduc L, Gurioli L, Harris A, Colò L, Rose-Koga EF (2015) Types and mechanisms of strombolian
 657 explosions: characterization of a gas-dominated explosion at Stromboli. *Bull Volcanol* 77(8). doi:
 658 10.1007/s00445-014-0888-5

659 Lu Z, Power JA, McConnell VS, Wicks C Jr, Dzurisin D (2002) Preeruptive inflation and surface
 660 interferometric coherence characteristics revealed by satellite radar interferometry at Makushin
 661 Volcano, Alaska: 1993–2000. *J Geophys Res* 107(B11):2266. doi: 10.1029/2001JB000970

662 Lu Z, Masterlark T, Dzurisin D, Rykhus R, Wicks C Jr (2003) Magma supply dynamics at
 663 Westdahl volcano, Alaska, modeled from satellite radar interferometry. *J Geophys Res*
 664 108(B7):2354. doi: 10.1029/2002JB002311

665 Lu Z, Dzurisin D, Biggs J, Wicks C Jr, McNutt S (2010) Ground surface deformation patterns,
 666 magma supply, and magma storage at Okmok volcano, Alaska, from InSAR analysis: 1.
 667 Intereruption deformation, 1997–2008. *J Geophys Res* 115(B5):B00B02. doi:
 668 10.1029/2009JB006969

669 Lube G, Cronin SJ, Platz T, Freundt A, Procter JN, Henderson C, Sheridan MF (2007) Flow and
 670 deposition of pyroclastic granular flows: A type example from the 1975 Ngauruhoe eruption, New
 671 Zealand. *J Volcanol Geotherm Res* 161:165-186

672 Luzi G, Pieraccini M, Mecatti D, Noferini L, Guidi G, Moia F, Atzeni C (2004) Ground-based radar
 673 interferometry for landslides monitoring: atmospheric and instrumental decorrelation sources on
 674 experimental data. *IEEE Trans Geosci Remote Sensing* 42:2454-2466

675 Macfarlane DG, Wadge G, Robertson DA, James MR, Pinkerton H (2006) Use of a portable
 676 topographic mapping millimetre wave radar at an active lava flow. *Geophys Res Lett* 33(3)
 677 (L03301). doi:10.1029/2005GL025005

678 Marchetti E, Genco R, Ripepe M (2009) Ground deformation and seismicity related to the
 679 propagation and drainage of the dyke feeding system during the 2007 effusive eruption at Stromboli
 680 volcano (Italy). *J Volcanol Geotherm Res* 182(3):155-161

681 Marsella M, Baldi P, Coltelli M, Fabris M (2012) The morphological evolution of the Sciara del
 682 Fuoco since 1868: reconstructing the effusive activity at Stromboli volcano. *Bull Volcanol*
 683 74(1):231-248

684 Martini M, Giudicepietro F, D'Auria L, Esposito AM, Caputo T, Curciotti R, De Cesare W, Orazi
 685 M, Scarpato G, Caputo A, Peluso R, Ricciolino P, Linde A, Sacks S (2007) Seismological
 686 monitoring of the February 2007 effusive eruption of the Stromboli volcano. *Annals of Geophysics*
 687 50(6):775-788

688 McGuire WJ, Pullen AD (1989) Location and orientation of eruptive fissures and feeder-dykes at
 689 Mount Etna; influence of gravitational and regional tectonic stress regimes. *J Volcanol Geotherm*
 690 *Res* 38:325-344

691 Melnik O, Sparks RSJ (2002) Dynamics of magma ascent and lava extrusion at Soufrière Hills
 692 Volcano, Montserrat. In: Druitt TH, Kokelaar BP (eds) *The Eruption of Soufrière Hills Volcano,*
 693 *Montserrat, from 1995 to 1999.* *Geol Soc London Memoirs* 21:153-171

694 Miyabuchi Y, Watanabe K, Egawa Y (2006) Bomb-rich basaltic pyroclastic flow deposit from
 695 Nakadake, Aso Volcano, southwestern Japan. *J Volcanol Geotherm Res* 155:90-103.
 696 doi:10.1016/j.jvolgeores.2006.02.007

697 Neri M, Lanzafame G (2009) Structural features of the 2007 Stromboli eruption. *J Volcanol*
698 *Geotherm Res* 182:137-144. doi:10.1016/j.jvolgeores.2008.07.021

699 Parcheta CE, Houghton BF, Swanson DA (2012) Hawaiian fissure fountains 1: decoding deposits—
700 episode 1 of the 1969–1974 Mauna Ulu eruption. *Bull Volcanol* 74:1729-1743

701 Patrick MR (2007) Dynamics of Strombolian ash plumes from thermal video: Motion, morphology,
702 and air entrainment. *J Geophys Res* 112(B06202). doi:10.1029/2006JB004387

703 Patrick MR, Anderson KR, Poland MP, Orr T, Swanson DA (2015) Lava lake level as a gauge of
704 magma reservoir pressure and eruptive hazard. *Geology* 43:831-834

705 Patrick MR, Harris AJL, Ripepe M, Dehn J, Rothery DA, Calvari S (2007) Strombolian explosive
706 styles and source conditions: insights from thermal (FLIR) video. *Bull Volcanol* 69:769-784.
707 doi:10.1007/s00445-006-0107-0

708 Petronis MS, Delcamp A, van Wyk de Vries B (2013) Magma emplacement into the Lemptégy
709 scoria cone (Chaîne Des Puys, France) explored with structural, anisotropy of magnetic
710 susceptibility, and Paleomagnetic data. *Bull Volcanol* 75(10):1-22

711 Pinel V, Poland MP, Hooper A (2014) Volcanology: Lessons learned from synthetic aperture radar
712 imagery. *J Volcanol Geotherm Res* 289:81-113

713 Pioli L, Rosi M, Calvari S, Spampinato L, Renzulli A, Di Roberto A (2008) The eruptive activity of
714 28 and 29 December 2002. In: Calvari S, Inguaggiato S, Puglisi G, Ripepe M, Rosi M (eds) *The*
715 *Stromboli volcano: An integrated study of the 2002-2003 Eruption*, American Geophysical Union
716 *Monograph Series* 182:105-116. doi: 101029/182GM10, ISBN 978-0-87590-447-4

717 Pistolesi M, Delle Donne D, Pioli L, Rosi M, Ripepe M (2011) The 15 March 2007 explosive crisis
718 at Stromboli volcano, Italy: assessing physical parameters through a multidisciplinary approach. *J*
719 *Geophys Res* 116(B12) (B12206). doi:10.1029/2011JB008527

720 Ripepe M, Marchetti E, Poggi P, Harris AJL, Fiaschi A, Ulivieri G (2004) Seismic, Acoustic, and
 721 Thermal Network Monitors the 2003 Eruption of Stromboli Volcano. EOS Transactions,
 722 85(35):329-336

723 Ripepe M, Delle Donne D, Lacanna G, Marchetti E, Ulivieri G (2009) The onset of the 2007
 724 Stromboli effusive eruption recorded by an integrated geophysical network. J Volcanol Geotherm
 725 Res 182:131-136. doi:10.1016/j.jvolgeores.2009.02.011

726 Rizzo AL, Federico C, Inguaggiato S, Sollami A, Tantillo M, Vita F, Bellomo S, Longo M, Grassa
 727 F, Liuzzo M (2015) The 2014 effusive eruption at Stromboli volcano (Italy): Inferences from soil
 728 CO₂ flux and ³He/⁴He ratio in thermal waters. Geophys Res Lett 42:2235–2243.
 729 doi:10.1002/2014GL062955

730 Rittmann A (1931) Der ausbruch des Stromboli am 11 September 1930. Zeitschrift für vulkanologie
 731 14:47-77. In German.

732 Robertson REA, Aspinall WP, Herd RA, Norton GE, Sparks RSJ, Young SR (2000) The 1995–
 733 1998 eruption of the Soufrière Hills volcano, Montserrat, WI. Phil Trans Royal Soc London, Series
 734 A, 358(1770):1619-1637

735 Rosi M, Bertagnini A, Harris AJL, Pioli L, Pistolesi M, Ripepe M (2006) A case history of
 736 paroxysmal explosion at Stromboli: timing and dynamics of the April 5, 2003 event. Earth Plan Sci
 737 Letters 243(3):594-606

738 Rosi M, Pistolesi M, Bertagnini A, Landi P, Pompilio M, Di Roberto A (2013) Stromboli volcano,
 739 Aeolian Islands (Italy): present eruptive activity and hazards. Geol Soc London Memoirs 37(1):473-
 740 490

741 Rudolf H, Leva D, Tarchi D, Sieber AJ (1999) A mobile and versatile SAR system. Proceedings of
 742 Geoscience and Remote Sensing Symposium, IGARSS 1999, Hamburg, 592-594.

743 Savov IP, Luhr J, Navarro-Ochoa C (2008) Petrology and geochemistry of lava and ash erupted
744 from Volcan Colima, Mexico, during 1998–2005. *J Volcanol Geotherm Res* 174:241-256

745 Slatcher N, James MR, Calvari S, Ganci G, Browning J (2015) Quantifying effusion rates at active
746 volcanoes through integrated time-lapse laser scanning and photography. *Remote Sensing* 7:14967-
747 14987. doi:10.3390/rs71114967

748 Spampinato L, Calvari S, Oppenheimer C, Boschi E (2011) Volcano surveillance using infrared
749 cameras. *Earth Science Review* 106:63-91. doi: 10.1016/j.earscirev.2011.01.003

750 Sparks RSJ, Barclay J, Calder ES, Herd RA, Komorowski J-C, Luckett R, Norton GE, Ritchie LJ,
751 Voight B, Woods AW (2002) Generation of a debris avalanche and violent pyroclastic density
752 current on 26 December (Boxing Day) 1997 at Soufrière Hills Volcano, Montserrat. In: Druitt TH
753 and Kokelaar BP (eds) *The Eruption of Soufrière Hills Volcano, Montserrat, from 1995 to 1999*.
754 *Geol Soc London Mem* 21:409-434.

755 Staudacher T, Ferrazzini V, Peltier A, Kowalski P, Boissier P, Catherine P, Lauret F, Massin F
756 (2009) The April 2007 eruption and the Dolomieu crater collapse, two major events at Piton de la
757 Fournaise (La Réunion Island, Indian Ocean). *J Volcanol Geotherm Res* 184:126-137.
758 doi:10.1016/j.jvolgeores.2008.11.005

759 Sumner JM (1998) Formation of clastogenic lava flows during fissure eruption and scoria cone
760 collapse: the 1986 eruption of Izu-Oshima Volcano, eastern Japan. *Bull Volcanol* 60:195-212

761 Tibaldi A (1996) Mutual influence of dyking and collapses at Stromboli volcano, Italy. In: McGuire
762 WJ, Jones AP, Neuberg J (eds) *Volcano Instability on the Earth and Other Planets*, *Geol Soc*
763 *Special Publ* 110:55-63

764 Tibaldi A (2001) Multiple sector collapses at Stromboli volcano, Italy: how they work. *Bull*
765 *Volcanol* 63:112-125. doi:10.1007/s004450100129

766 Tommasi P, Baldi P, Chiocci F, Coltelli M, Marsella M, Pompilio M, Romagnoli C (2005) The
 767 Landslide Sequence Induced by the 2002 Eruption at Stromboli Volcano. In: Sassa K, Fukuoka H,
 768 Wang FW, Wang G (eds) Landslide - Risk analysis and sustainable disaster management. Springer
 769 Verlag 251-258. ISBN: 3-540-28664-0

770 Voight B, Komorowski J-C, Norton GE, Belousov AB, Belousova M, Boudon G, Francis PW,
 771 Franz W, Heinrich P, Sparks RSJ, Young SR (2002) The 26 December (Boxing Day) 1997 sector
 772 collapse and debris avalanche at Soufrière Hills Volcano, Montserrat. In: Druitt TH and Kokelaar
 773 BP (eds) The Eruption of Soufrière Hills Volcano, Montserrat, from 1995 to 1999. Geol Soc
 774 London Mem 21:363-407

775 Wadge G, Cole P, Stinton A, Komorowski JC, Stewart R, Toombs AC, Legendre Y (2011) Rapid
 776 topographic change measured by high-resolution satellite radar at Soufriere Hills Volcano,
 777 Montserrat, 2008–2010. J Volcanol Geotherm Res 199(1):142-152

778 Wadge G, Haynes M (1998) Cover Radar images growth of Soufriere Hills Volcano, Montserrat.
 779 Int J Rem Sens 19(5):797-800

780 Wadge G, Macfarlane DG, Odbert HM, James MR, Hole JK, Ryan G, Bass V, De Angelis S,
 781 Pinkerton H, Robertson DA, Loughlin SC (2008) Lava dome growth and mass wasting measured
 782 by a time series of ground-based radar and seismicity observations. J Geophys Res 113(B8)
 783 (B08210). doi:10.1029/2007JB005466

784 Wadge G, Macfarlane DG, Odbert HM, Stinton A, Robertson DA, James MR, Pinkerton H (2014)
 785 AVTIS observations of lava dome growth at Soufrière Hills Volcano, Montserrat: 2004 to 2011.
 786 Geol Soc London Memoirs 39(1):229-240

787 Wadge G, Scheuchl B, Stevens NF (2002) Spaceborne radar measurements of the eruption of
 788 Soufriere Hills Volcano, Montserrat. Geol Soc London Memoirs 21(1):583-594

789 Wadsworth FB, Kennedy BM, Branney MJ, von Aulock FW, Lavallé Y, Menendez A (2015)
790 Exhumed conduit records magma ascent and drain-back during a Strombolian eruption at Tongariro
791 volcano, New Zealand. Bull Volcanol 77:71. doi: 10.1007/s00445-015-0962-7

792 Zebker HA, Rosen PA, Hensley S (1997) Atmospheric effects in interferometric synthetic aperture
793 radar surface deformation and topographic maps. J Geoph Res 102(B4):7547-7563

794

795 **Figure captions**

796 **Figure 1.** a) Stromboli and the Aeolian Archipelago in Southern Italy. b) Perspective view of
797 Stromboli Island from the north. Locations and fields of view of the GBInSAR and of the visible
798 (SQV400) and thermal (SQT400) cameras used for this study are indicated by the triangles. c) View
799 from north of the summit area of Stromboli volcano, comprising the summit crater terrace and the
800 talus below the North-East crater area (NEC talus). In the crater terrace three different vent areas
801 were identified: the North-East crater (NEC), Central Crater (CC) and South-West crater (SWC).
802 Within the NEC area three different vents were recognized: NEC1, NEC2 and NEC hornito. The
803 background topographic data are represented by a very high resolution Digital Elevation Model
804 (DEM) with a spatial resolution of 50 cm. This DEM was obtained by elaborating the 3D data (8
805 pt/m²) acquired during the airborne laser scanning survey carried out from 4 to 18 May 2012 by
806 BLOM Compagnia Generale Riprese aeree S.P.A. (www.blomasa.com). The data were acquired
807 using the Leica ADS80 sensor, whose instrumental vertical and horizontal accuracy is $\pm 10/20$ cm
808 and ± 25 cm, respectively. The map was generated using an ESRI platform.

809

810 **Figure 2.** GBInSAR interferogram calculated between 12 and 13 January 2013 (left) and coherence
811 map calculated for the same period (right) highlighting high-coherence areas (yellow in the
812 coherence map to the right, red in the interferogram on the left), where displacements are
813 measurable, and low-coherence areas, where morphological changes were measured through power
814 image analysis (speckled areas on both the interferogram and the coherence map).

815

816 **Figure 3.** a) View of the vent area overlaid with the GBInSAR cumulative displacement map
817 between 24 December 2012 and 15 January 2013. Negative (yellow and red) and positive (blue)

818 values represent movement towards and away from the sensor, respectively, corresponding to
819 inflation and deflation of the summit portion of the volcano. The movement of the reference point
820 of this portion (black dot) is represented in Fig. 4b. The inset on the upper left of the image shows
821 the crater area (red outline) whose variability is shown in Fig. 4c. b) GBInSAR cumulative
822 displacement time series relative to the vents area. The occurrence of overflows is also reported.
823 The time-series analysis revealed that the 12 January 2013 crater-wall collapse occurred in a period
824 of long-term inflation. The only remarkable deflation occurred soon after the crater-wall collapse,
825 as a consequence of the 13 to 15 January overflows.

826

827 **Figure 4.** a) 1 January 2013 visible image recorded at 08:16 from the SQV camera. The vertical
828 field of view is ~700 m. The yellow square indicates the area framed (and magnified) by thermal
829 and visual images b, c, e. b) 11 January 2013 thermal image recorded at 09:01:52 showing two
830 small lava flows erupted from vents at the base of the NEC wall, and a powerful explosion taking
831 place from the NEC hornito. c) 12 January 2013 visible image (magnified) recorded at 00:08:16,
832 showing a lava flow emerging from the saddle on the NEC crater rim, and two vents at the base of
833 the NEC wall. Explosions taking place within the NEC were visible through the vents on the E rim
834 of the NEC, testifying that the crater rim, made up of loose spatter rapidly accumulated during the
835 powerful explosive activity occurring before the 12 January crater-wall collapse, was fractured. d)
836 12 January 2013 visible image (real size, same as a) recorded at 04:17:44, showing powerful
837 explosions from NEC, a lava flow emerging from the saddle of the crater rim, and bombs fallout
838 and small landslides occurring from the crater rim and causing incandescent landslides on the NEC
839 outer flanks triggered by spatter fallout. e) 12 January 2013 thermal image, recorded at 05:44:28,
840 showing a strong explosion from NEC and a lava flow spreading along the SdF. f) 13 January 2013
841 visible image (magnified), recorded at 08:07:42, displaying the morphological change of the NEC
842 crater rim resulting from crater-wall failure. g) Photo courtesy of Domenico Mangione (DPC) taken

843 from NE on 14 January 2013 displaying the crater wall made up of loose spatter, the NEC-hornito,
844 and the new crater rim (shown by yellow arrows) following the 12 January crater-wall collapse.

845 **Figure 5.** Multiparameter plot of summit cone behaviour from 8 December 2012 to 8 March 2013.
846 The five phases that we have recognised in this period are indicated by Roman numerals. The
847 occurrence of overflows is shown with red triangles, and the 12 January 2013 crater-wall collapse is
848 indicated with the black arrow. a) Explosion rate time series measured by the SQT400 thermal
849 camera. b) Daily displacement time series along the GBInSAR line of sight (LOS, Fig. 2a), which is
850 representative of the behaviour of the NEC summit cone. Negative and positive values of
851 displacement indicate, respectively, a movement toward and away from the sensor corresponding to
852 either inflation (negative values) or deflation (positive values) of the summit cone (Di Traglia et al.
853 2014b). Data were standardized ($x_n = x_u\mu/\sigma$; where x_n is the standardized data, x_u is the original
854 data, μ is the mean and σ is the standard deviation of the time series). Horizontal lines at ± 1 and ± 2
855 represent σ and 2σ of the standardized time-series, respectively. Significant short-term inflation
856 episodes were recorded in the periods: 20-22 December 2012, 15 February 2013 and from 28
857 February 2013 until the end of the considered period (8 March 2013). Noteworthy short-term
858 deflation occurred in the periods: 26-30 December 2012 and 12-18 January 2013. The last short-
859 term deflation was the strongest of the entire analysed period. c) Daily NEC area measured using
860 GBInSAR power images. The 12 January 2013 crater-wall collapse occurred in a period of fast
861 crater enlargement, owing to the weakening and erosion due to the on-going eruptive activity.

862

863

864

865

866

867

868

869

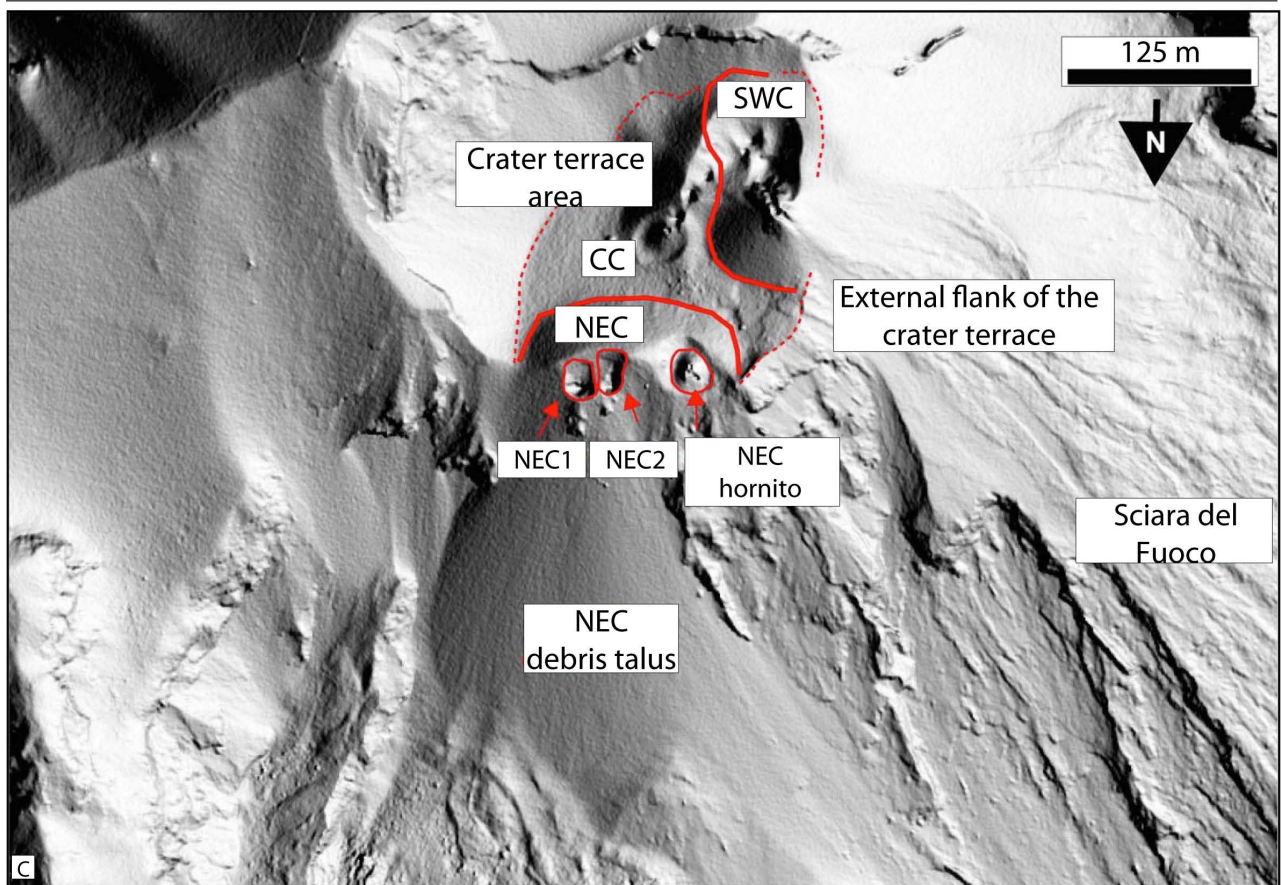
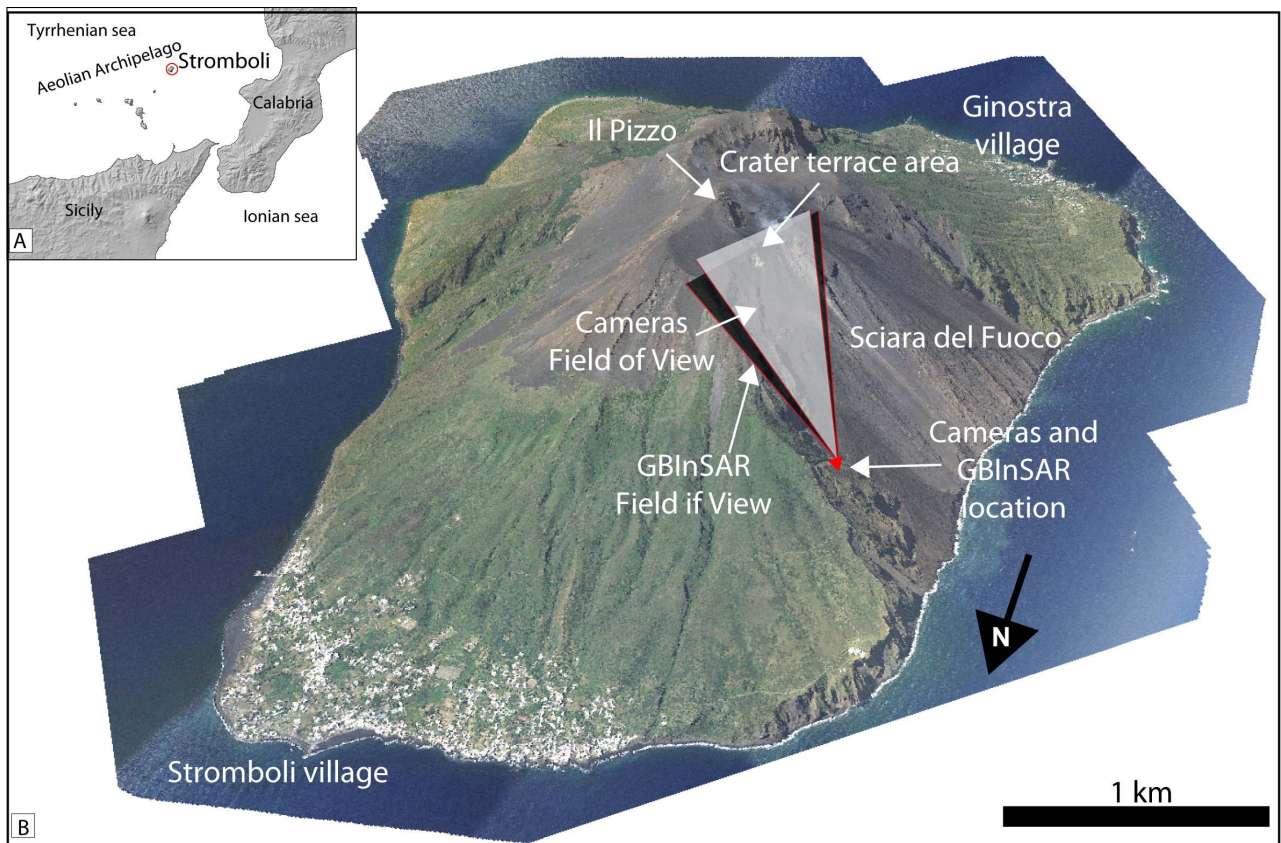
870 **Table 1** - Comparison among key parameters of crater-wall collapse deposits at Stromboli and other
871 volcanoes

Volcano	Date	Deposit	Size	Notes	Reference
Vesuvius	1944	Avalanche	1.3 km long and $\sim 1 \times 10^6 \text{ m}^3$ in volume	Occurred after several lava fountains and triggered by seismicity where lava and pyroclastics loaded the slopes	Hazlett et al. 1991; Cole and Scarpati 2010;
Stromboli	1985	Small hot avalanche	unknown	Followed the opening of an eruptive fissure on the NE flank of the summit cone	De Fino et al. 1988
Arenal	1987-2001	Pyroclastic flows	up to 3.0 km long and $2.2 \pm 0.8 \times 10^6 \text{ m}^3$ in volume	Generated by column collapse, crater-wall collapse, and lava flow output from the summit pool	Alvarado and Soto 2002; Cole et al. 2005
Montserrat	1997	Pyroclastic flows and debris avalanches	up to 7 km long and up to $50 \times 10^6 \text{ m}^3$ in volume	Dome and crater-wall collapses generated by gravitational instability; great erosive capacity; larger flows breached the valley walls	Cole et al. 1998, 2002; Sparks et al. 2002; Voight et al. 2002
Etna	1999	Pyroclastic avalanches, hot mass flows and avalanches, rock falls	up to 0.7 km long	Following a period of intense explosive activity and generated by gravitational instability of pyroclastics and of a summit lava dome and involving outward thrusting of a section of the Bocca Nuova crater rim	Calvari and Pinkerton 2002; Behncke et al. 2003
Stromboli	2002	Hot avalanche	20 m thick close to the vents, 4-5 m thick at the coast, $\sim 1.7 \text{ km}$ away	Accompanied the opening of an eruptive fissure on the NE flank of the summit cone, and formed a deposit that reached the shoreline (1.7 km away) where it was $\sim 4\text{-m-thick}$	Calvari et al. 2005; Lodato et al. 2007; Pioli et al. 2008
Etna	2006	Pyroclastic density currents	up to 1 km long	Collapse of parts of the SE-Crater during the opening of a large fracture on the flank of the cone	Behncke et al. 2008
Stromboli	2007	Landslides of hot debris	Unknown	Inflation of the summit cone climaxed with landslides along the SdF, dike intrusion, breaching of the summit cone, localized inflation, and effusive vent opening at 400 m a.s.l.	Martini et al. 2007; Casagli et al. 2009; Marchetti et al. 2009; Calvari et al. 2010
Stromboli	2014	Unknown	Unknown	Increase in the rate of displacement at the summit and eruptive fissure	Di Traglia et al. 2015; Rizzo et

				opening on the NE flank of the summit cone	al. 2015
--	--	--	--	---	----------

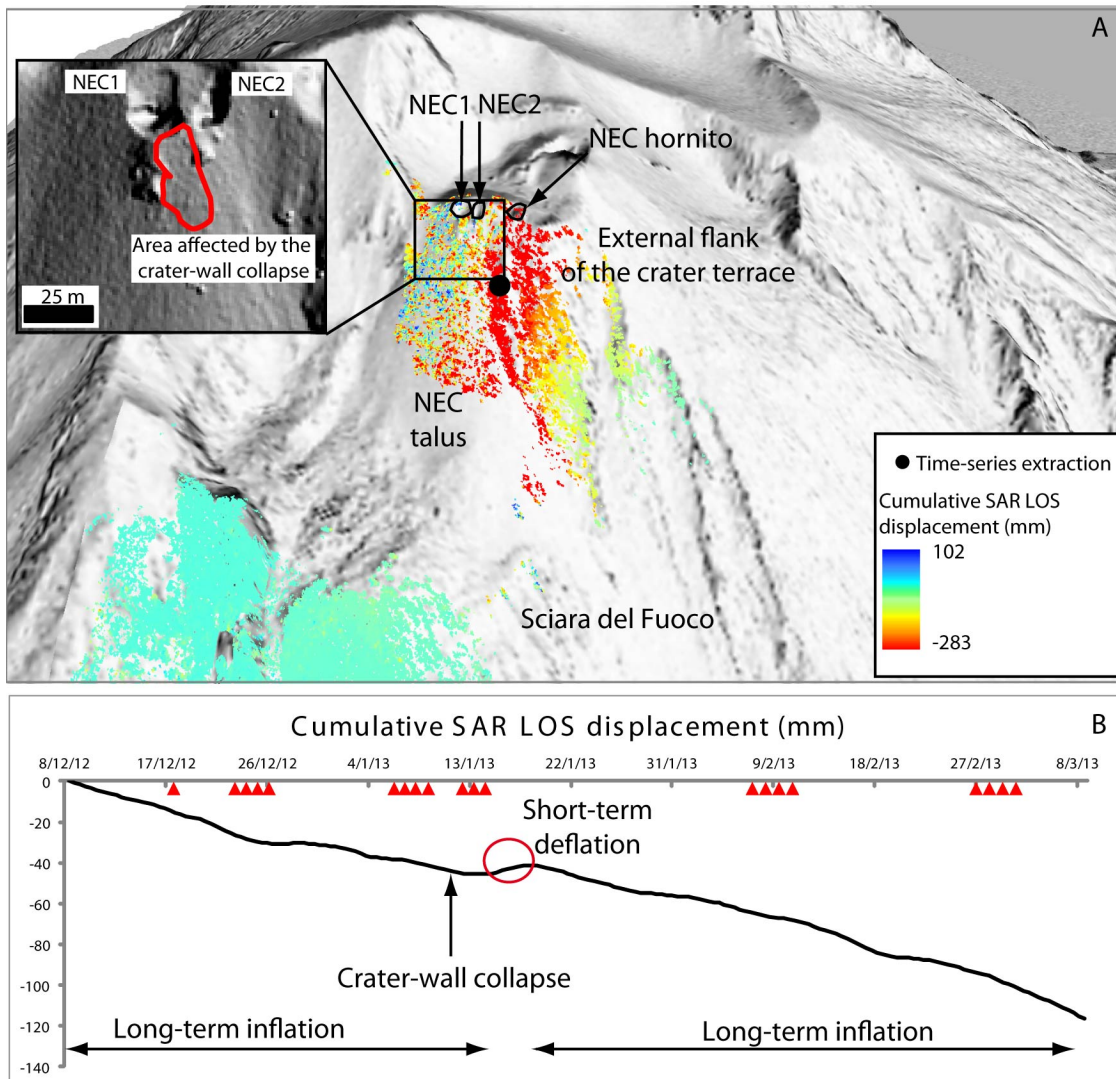
872

873



874

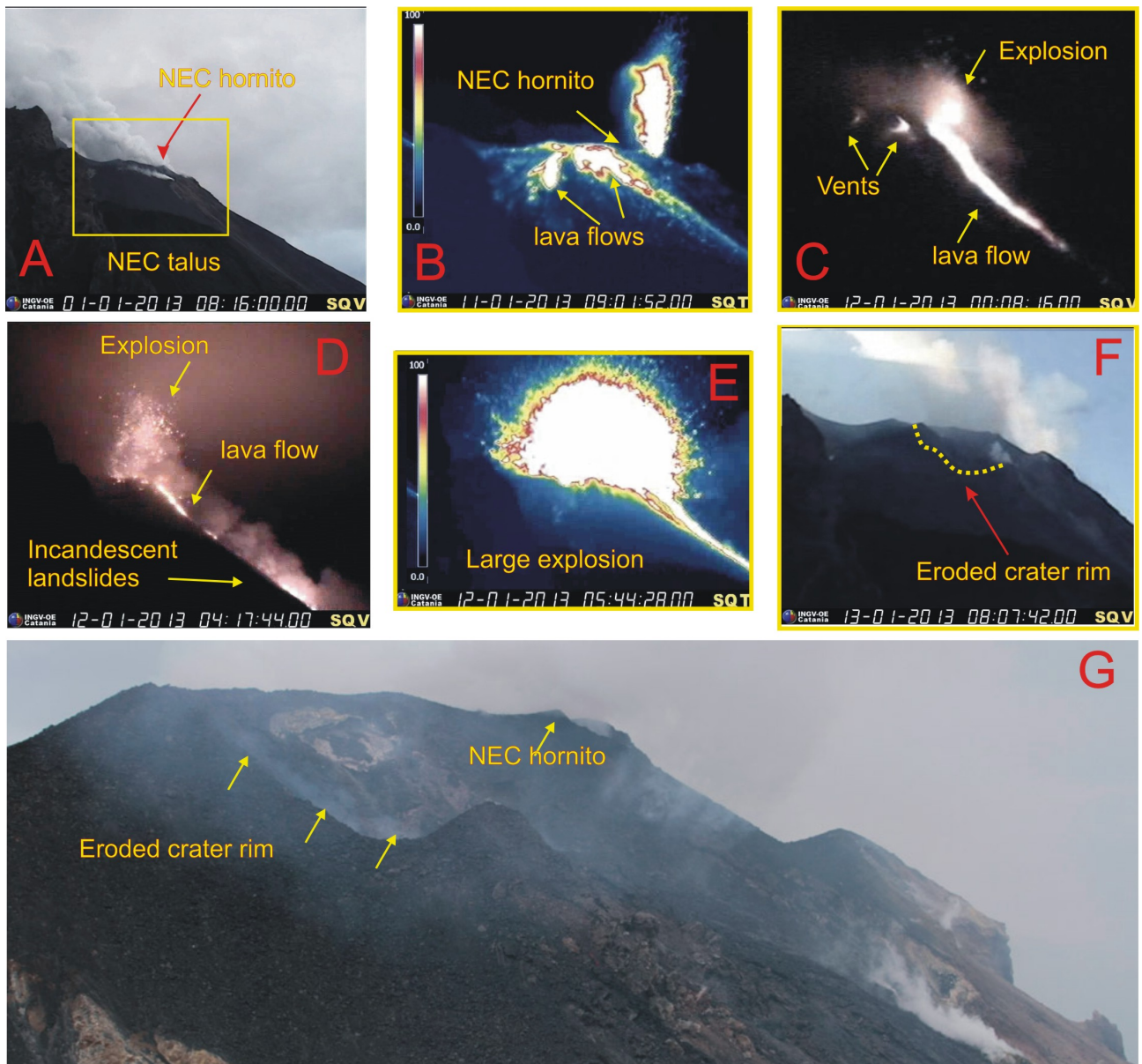
875 Figure 1



876

877 Figure 2

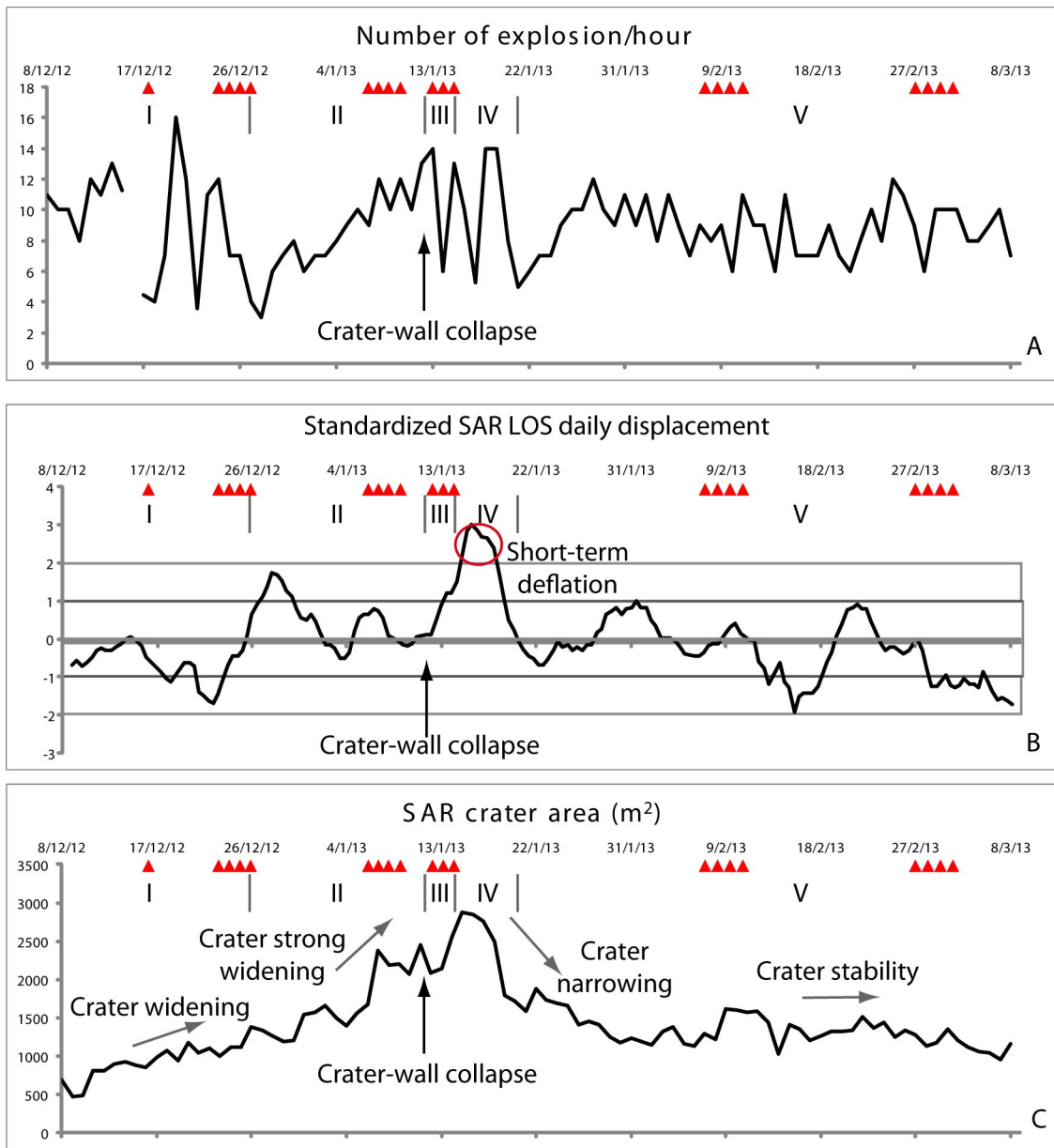
878



879

880 Figure 3

881



882

883 Figure 4

884

885 Supplementary Material for

886 **Monitoring crater-wall collapse and pyroclastic density currents at active volcanoes: a study of the 12**
887 **January 2013 event at Stromboli**

888 Calvari S.^{1,*}, Intrieri E.², Di Traglia F.², Bonaccorso A.¹, Casagli N.², Cristaldi A.¹

889 1 - Istituto Nazionale di Geofisica e Vulcanologia, Osservatorio Etneo - Sezione di Catania, Piazza Roma 2,
890 95125 Catania, Italy

891 2 - Dipartimento di Scienze della Terra, Università di Firenze, Via La Pira 4, 50121, Firenze, Italy

892

893 1. **Methods**

894 1.1 *Webcam network*

895 The observation of eruptive activity at Stromboli is carried out using the Istituto Nazionale di Geofisica e
896 Vulcanologia - Osservatorio Etneo (INGV-OE) webcams monitoring network. This comprises thermal
897 infrared (~8-14 μm) and visible (400-700 nm) cameras located at Il Pizzo (Fig. 1B), at 900 m elevation and
898 ~250 m from the craters, plus visible and thermal infrared cameras (respectively SQV400 and SQT400) at
899 400 m elevation on the N flank of the SdF and ~800 m from the craters (Figure 1B). During January-March
900 2013, the recording of the eruptive events was done using the SQV400 and SQT400 cameras, which view the
901 NEC and the upper eastern sector of the SdF from NE (Fig. 1B). To obtain a description of the eruptive
902 activity, the total number of explosive events that occurred during each day of cloud-free observation was
903 manually counted and reported as an integer average hour value (Fig. 4A). On average, 5-9% of the days
904 were affected by clouds and/or by system failure. In such cases data are lacking.

905

906 1.2 *The GBInSAR monitoring system*

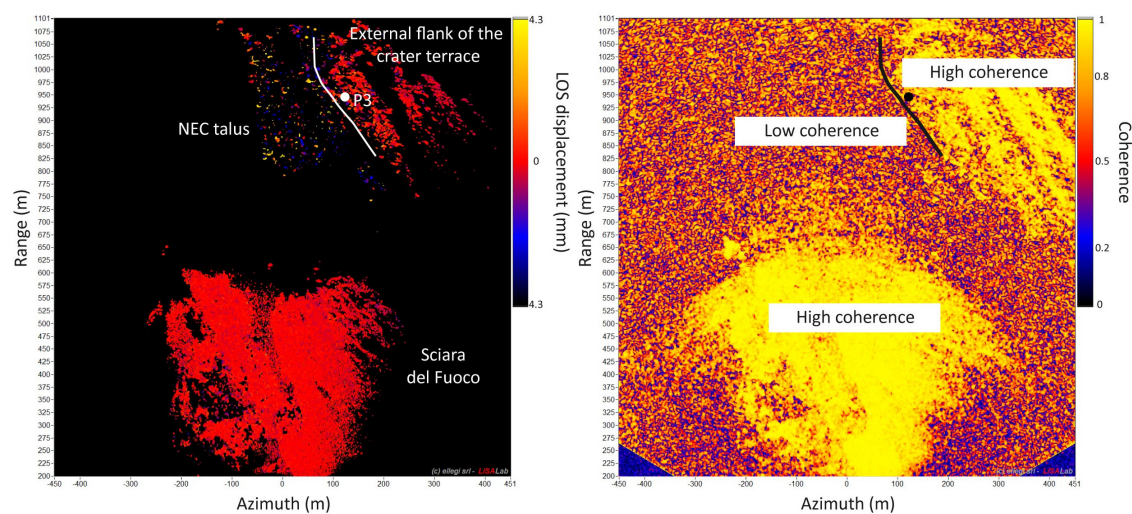
907 The NE portion of the crater terrace of Stromboli (Figure 1B-C) has been monitored since January
908 2003 (Casagli et al. 2009; Di Traglia et al. 2014b) by a GBInSAR system located in a stable area
909 outside the SdF and ~ 1.5 km from the crater terrace (Figure 1B). A GBInSAR is a remote sensing
910 instrument consisting of a transmitting and a receiving antenna that emits microwaves and records
911 the amplitude and phase of the backscattered signal (Rudolf et al. 1999; Luzi et al. 2004). The
912 capability of SAR interferometry to measure volcano deformation depends on the persistence of
913 phase coherence over the investigated time intervals (Lu et al. 2002, 2010), and also on the type of
914 surface material, which is an important factor affecting interferometric coherence (Lu et al. 2002,
915 2003). The loss in coherence is primarily due to fast ground movements, such as the emplacement
916 of lava flows or debris avalanches (Di Traglia et al. 2013, 2014b). Here, the loss in phase coherence
917 is used to delimit the area affected by continuous erosion/deposition of material from areas
918 influenced by volcano deformation. Areas of high coherence are the external flank of the crater
919 terrace and the Sciara del Fuoco (Fig. SM1), whereas the NEC talus (Fig. 1C) shows very low
920 coherence even at short-interval interferograms (< 1 day). Moreover, for interferometric analysis a
921 coherence threshold equal to or above 0.8 is required to consider the information on the deformation
922 reliable (Di Traglia et al. 2014b).

923 The amplitude is proportional to the energy reflected by the targets and depends on characteristics such as
924 dielectric properties of the reflecting materials, their orientation with respect to the receiving antenna (which
925 is in turn related to the smoothness or roughness of the surfaces) and meteorological conditions. From
926 amplitude squared it is possible to produce power images. They are useful to observe and quantify
927 geomorphological changes of a topographic surface (Wadge and Haynes 1997; Macfarlane et al. 2006;
928 Wadge et al. 2002, 2008, 2011, 2014), such as, for the case of Stromboli, formation and changes of the NEC
929 notch or growth of NEC talus (Di Traglia et al. 2014a).

930 In order to quantitatively evaluate the changes in the NEC's morphology, daily-averaged power images
931 produced by the GBInSAR were used. The system produces an image every 11 minutes, therefore ~ 130 of

932 them are used to form an averaged one. This process increases the signal to noise ratio and therefore
933 facilitates the interpretation. Since the NEC rim produces a shadow zone corresponding to the crater
934 depression, it is possible to calculate the area of the crater itself as it changes over time (Fig. 2A). The
935 precision of the measurements is affected by pixels size (increasing with distance) and by the amplitude of
936 the backscattered signals, which is not constant with time, thus causing uncertainty when determining the
937 boundary of the crater area. When the areal extent of the crater depression can be assumed stable (that is
938 during periods of lower volcanic activity) it is possible to calculate the precision (standard deviation) of such
939 method. For this application the standard deviation has been calculated equal to 80 m. To map the area
940 affected by the 12 January crater-wall collapse, a threshold was set at ~55 dB.

941 In the configuration deployed at Stromboli, the antenna moves along a 3 m-long rail (Di Traglia et al.
942 2014b). Working in Ku band (17.0-17.1 mm), it has the advantage of penetrating dust clouds and working in
943 any light and atmospheric condition. The GBInSAR measures ground displacement in its field-of-view
944 (FOV; Fig. 1B) along the line of sight (LOS, Fig. 2A; average azimuth angle=15°) by computing, via cross
945 correlation, the phase differences between the backscattered signals associated with two consecutive
946 synthetic aperture radar images. The phase is elaborated with interferometric techniques to retrieve the
947 displacement of the investigated area occurring between two acquisitions. Both the range and cross-range
948 resolutions are on average 2 m × 2 m, with a precision in displacement measurements of less than 1 mm.
949 Negative and positive values of displacement indicate, respectively, a movement toward and away from the
950 sensor corresponding to either inflation (negative values) or deflation (positive values) of the summit cone
951 (Di Traglia et al. 2014b). The system combines all the 8-hours averaged images, “stacking” the phase of the
952 formed interferograms (Zebker et al. 1997; Antonello et al. 2004; Intrieri et al. 2013; Di Traglia et al.
953 2014c). Interferometric stacks highlights persistent deformation whereas other random signals, like
954 atmospheric anomalies, are suppressed (Pinel et al. 2014). This approach is appropriate when the
955 deformation is episodic with no change in source parameters over time, as observed at Stromboli by Di
956 Traglia et al. (2015). The time series extracted in this study derives from GBInSAR P3 control point (black
957 dot in Fig. 2A) located on a high-coherence area (the external part of the crater terrace), whose
958 measurements over time have displayed the best consistency and accuracy.



960

961 Figure SM1. GBInSAR interferogram calculated between 12 and 13 January 2013 (left) and
962 coherence map calculated along the same period (right) highlighting high-coherence areas (yellow
963 in the coherence map to the right, red in the interferogram on the left), where displacements are
964 measurable, and low-coherence areas, where morphological changes were measured through power
965 image analysis (speckled areas on both the interferogram and the coherence map).

966

967

968

969

970

971

972 **Reference list**

973 Di Traglia F, Ventisette C, Rosi M, Mugnai F, Intrieri E, Moretti S, Casagli N (2013) Ground-based
974 InSAR reveals conduit pressurization pulses at Stromboli volcano. *Terra Nova* 25(3):192-198

975

976 Di Traglia F, Nolesini T, Intrieri E, Mugnai F, Leva D, Rosi M, Casagli N (2014) Review of ten
977 years of volcano deformations recorded by the ground-based InSAR monitoring system at

978 Stromboli volcano: a tool to mitigate volcano flank dynamics and intense volcanic activity. Earth
979 Science Reviews 139:317-335

980

981 Lu Z, Power JA, McConnell VS, Wicks C Jr, Dzurisin D (2002) Preeruptive inflation and surface
982 interferometric coherence characteristics revealed by satellite radar interferometry at Makushin
983 Volcano, Alaska: 1993–2000. J Geophys Res 107(B11):2266. doi: 10.1029/2001JB000970

984

985 Lu Z, Masterlark T, Dzurisin D, Rykhus R, Wicks C Jr (2003) Magma supply dynamics at
986 Westdahl volcano, Alaska, modeled from satellite radar interferometry. J Geophys Res
987 108(B7):2354. doi: 10.1029/2002JB002311

988

989 Lu Z, Dzurisin D, Biggs J, Wicks C Jr, McNutt S (2010) Ground surface deformation patterns,
990 magma supply, and magma storage at Okmok volcano, Alaska, from InSAR analysis: 1.
991 Intereruption deformation, 1997–2008. J Geophys Res 115(B5):B00B02. doi:
992 10.1029/2009JB006969

993 Luzi G, Pieraccini M, Mecatti D, Noferini L, Guidi G, Moia F, Atzeni C (2004) Ground-based radar
994 interferometry for landslides monitoring: atmospheric and instrumental decorrelation sources on
995 experimental data. IEEE Trans Geosci Remote Sensing 42:2454-2466

996

997 Macfarlane DG, Wadge G, Robertson DA, James MR, Pinkerton H (2006) Use of a portable
998 topographic mapping millimetre wave radar at an active lava flow. Geophys Res Lett 33(3):L03301.
999 doi:10.1029/2005GL025005

1000

1001 Rudolf H, Leva D, Tarchi D, Sieber AJ (1999) A mobile and versatile SAR system. Proceedings of
1002 Geoscience and Remote Sensing Symposium, IGARSS 1999, Hamburg, 592-594.

1003

1004 Wadge G, Macfarlane DG, Odbert HM, James MR, Hole JK, Ryan G, Bass V, De Angelis S,
1005 Pinkerton H, Robertson DA, Loughlin SC (2008) Lava dome growth and mass wasting measured by
1006 a time series of ground- based radar and seismicity observations. J Geophys Res 113(B8):B08210.
1007 doi:10.1029/2007JB005466
1008
1009 Wadge G, Macfarlane DG, Odbert HM, Stinton A, Robertson DA, James MR, Pinkerton H (2014)
1010 AVTIS observations of lava dome growth at Soufrière Hills Volcano, Montserrat: 2004 to 2011.
1011 Geol Soc London Memoirs 39(1):229-240
1012
1013